University of KwaZulu-Natal
College of Agriculture, Engineering and Science

Automatic Lung Segmentation using Graph Cut optimization

by:

Oluwakorede Monica Oluyide

213554623

Supervisors:

Prof. Serestina Viriri

Prof. Jules-Raymond Tapamo

in fulfillment of the academic requirements for the degree of Master of Science in Computer Science, School of Mathematics, Statistics and Computer Science, University of KwaZulu-Natal

Submitted 6th February, 2015

Abstract

Medical Imaging revolutionized the practice of diagnostic medicine by providing a means of visualizing the internal organs and structure of the body. Computer technologies have played an increasing role in the acquisition and handling, storage and transmission of these images. Due to further advances in computer technology, research efforts have turned towards adopting computers as assistants in detecting and diagnosing diseases, resulting in the incorporation of Computer-aided Detection (CAD) systems in medical practice. Computed Tomography (CT) images have been shown to improve accuracy of diagnosis in pulmonary imaging. Segmentation is an important preprocessing necessary for high performance of the CAD. Lung segmentation is used to isolate the lungs for further analysis and has the advantage of reducing the search space and computation time involved in disease detection.

This dissertation presents an automatic lung segmentation method using Graph Cut optimization. Graph Cut produces globally optimal solutions by modeling the image data and spatial relationship among the pixels. Several objects in the thoracic CT image have similar pixel values to the lungs, and the global solutions of Graph Cut produce segmentation results where the lungs, and all other objects similar in intensity value to the lungs, are included. A distance prior encoding the euclidean distance of pixels from the set of pixels belonging to the object of interest is proposed to constrain the solution space of the Graph Cut algorithm. A segmentation method using the distance-constrained Graph Cut energy is also proposed to isolate the lungs in the image. The results indicate the suitability of the distance prior as a constraint for Graph Cut and shows the effectiveness of the proposed segmentation method in accurately segmenting the lungs from a CT image.

Preface

This research discussed in this dissertation was done at the University of KwaZulu-Natal, Durban from February 2013 to February 2015 by Oluwakorede Monica Oluyide under the supervision of Prof. Serestina Viriri and Prof. Jules-Raymond Tapamo.

Declaration - Supervisor

As the candidate's supervisor, I agree to the submission of this dissertation

---

Prof. Serestina Viriri

Declaration - Co-Supervisor

As the candidate's co-supervisor, I agree to the submission of this dissertation

---

Prof. Jules-Raymond Tapamo

Declaration - Plaigiarism

I, Oluwakorede Monica Oluyide, declare that

1. The research reported in this dissertation, except where otherwise indicated, is my original research.
2. This dissertation has not been submitted for any degree or examination at any other university.
3. This dissertation does not contain other persons' data, pictures, graphs or other information, unless specifically acknowledged as being sourced from other persons.
4. This dissertation does not contain other persons' writing, unless specifically acknowledged as being sourced from other researchers. Where other written sources have been quoted, then:
   (a) Their words have been re-written but the general information attributed to them has been referenced
   (b) Where their exact words have been used, then their writing has been placed in italics and inside quotation marks, and referenced.
5. This dissertation does not contain text, graphics or tables copied and pasted from the Internet, unless specifically acknowledged, and the source being detailed in the dissertation and in the References sections.

Oluwakorede Monica Oluyide

Declaration - Publications

DETAILS OF CONTRIBUTION TO PUBLICATIONS that form part and/or include research presented in this dissertation

Publication 1:

Oluwakorede Oluyide, Serestina Viriri, and Jules-Raymond Tapamo. A Two-Stage Fuzzy c-Means Clustering Algorithm for Lung Segmentation. *In Proceedings of the 2014 PRASA, RobMech and AfIaT International Joint Symposium, Cape Town, South Africa*, pages 49–52, Nov 2014

Oluwakorede Monica Oluyide

Acknowledgments

I want to express my profound gratitude to my supervisors, Prof. Serestina Viriri and Prof. Jules-Raymond Tapamo for their words of encouragement, dedication and commitment throughout the Master's degree program.

I am deeply grateful to my family for their love and support and for always being there for me.

My sincere thanks go to my friends, especially those I met in the course of this Masters, whose kind words and work ethics served as an inspiration to keep striving to be the best I can be.

I am extremely grateful to God for the abundant graces and blessings He has been showering on me.

Contents

List of Figures

List of Tables

Abbreviations

CT	**C**omputed **T**omography
CAD	**C**omputer **A**ided **D**etection
FCM	**F**uzzy **c** **M**eans
DICOM	**D**igital **I**maging and **CO**mmunication in **M**edicine
PACS	**P**icture **A**rchiving and **C**ommunication **S**ystem
RIS	**R**adiology **I**nformation **S**ystems
SSCT	**S**ingle **S**lice **C**omputed **T**omography
MSCT	**M**ulti **S**lice **C**omputed **T**omography
MDCT	**M**ulti **D**etector **C**omputed **T**omography
HU	**H**ounsfield **U**nits
GSS	**G**aussian **S**cale **S**pace
RASM	**R**obust **A**ctive **S**hape **M**atching
MGRF	**M**arkov **G**ibbs **R**andom **F**ield
MRF	**M**arkov **R**andom **F**ield
MAP	**M**aximum **a** **P**osteriori
DCE	**D**istance **C**onstrained **E**nergy
LIDC-IDRI	**L**ung **I**mage **D**atabase **C**onsortium and **I**mage **D**atabase **R**esource **I**nitiative
LungTIME	**Lung** **T**est **I**mages from **M**otol **E**nvironment
DC	**D**ice **C**oefficient
JS	**J**accard **S**imilarity
GT	**G**round **T**ruth
SR	**S**egmentation **R**esult
TP	**T**rue **P**ositive

TN	**T**rue **N**egative
FN	**F**alse **N**egative
FP	**F**alse **P**ositive

Chapter 1

General Introduction

1.1 Introduction

The discovery of x-rays by Wilhelm Roentgen [3] in 1895 revolutionized the practice of diagnostic medicine and gave rise to the field of radiology which involves the use of imaging technologies to perform diagnosis and administer treatments [4, 5]. Imaging technologies provide non-invasive ways of viewing the interior of the body and produce detailed images of the structure of organs and the skeleton within the body. Computed Tomography (CT), an imaging technology, invented in 1972 by Godfrey Hounsfield [6] uses x-rays to produce two-dimensional slices of a part of the body by placing the body through a ring of x-ray tubes and detectors. The principle behind this x-ray imaging modality is that various parts of the body absorb x-rays differently depending on their densities; images are formed based on the amount of radiation absorbed, and the higher the density of the body part, the higher the amount of x-rays absorbed and the higher the intensity value in the resulting image. According to Linton [7], the order of decreasing density of the anatomical parts of the body is as follows: bones, soft tissue, fat, and air. The bones of the body are very dense and absorb most of the radiation. This causes the bone region to appear white on an x-ray image. The soft tissues of the body contain water, and are less dense

than the bone. This allows more radiation to pass through and as a result, the tissues appears gray on the image. Fat is less dense than water and appears less grayish. Air is the least dense and appears almost black on the image because it allows almost all of the x-rays to pass through. To form the CT slices, the x-rays are projected from different angles onto the body and the amount of radiation absorbed is recorded by the detectors. These slices are two dimensional in nature, and can be stacked together to produce three dimensional views of the body. The measurements from the different detectors are used to form the images on a computer.

Computers have been an integral part of modern radiology. They are used to compose and format medical reports by combining text and images from various modalities [8]. The use of Picture Archiving and Communication Systems (PACS) has became an invaluable way of storing and archiving images from different modalities. Standards such as Digital Imaging and Communication in Medicine (DICOM) were created to ensure proper handling, storage, printing and transmission of medical images [9]. Individual workstations allowed images to be accessed by the physicians, modified and stored for later use. Teleradiology provides an efficient means of transmission of images across different locations [10].

As the role of computers extended to acquiring, displaying and archiving images, the possibility of using computers in other areas of diagnosis arose [11]. Studies were carried out seeking to transform it into a diagnostician [12–14] as it was hoped that computers would be able to independently identify images with abnormalities from the normal images, and then perform the interpretive process of a physician on each image and output the diagnosis. The interpretive process can be divided into three steps: detection, description and differential diagnosis [11]. One of the several obstacles that hindered the realization of automated diagnosis was the inability of experts to explicitly define the reason behind their own decision–making, and this, in turn, led to difficulty in creating an effective set of rules to guide decision–making [14]. In addition, there was a lack of mature computer algorithms at the time to handle tasks of such complexity [15]. Therefore, a greater

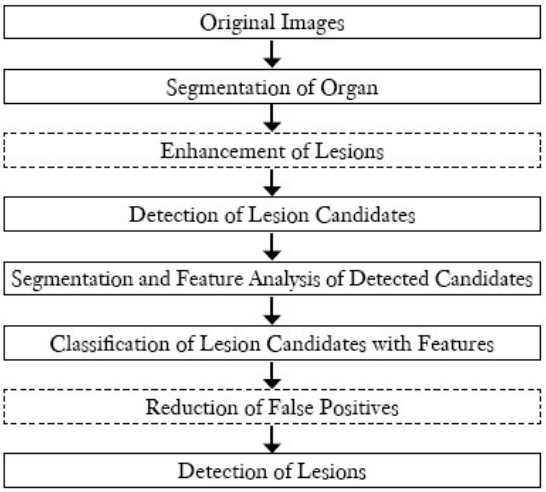

FIGURE 1.1: A typical flow diagram for a CAD system for lesion detection in thoracic images. Boxes with solid line are the major steps in CAD while the boxes with dashed lines are the optional steps. From [23]

volume of research turned towards using the computer to assist in making more accurate diagnoses [15–23].

Automation of the detection step in the interpretive process is usually done with Computer-Aided Detection (CAD) systems using image processing and pattern recognition algorithms to highlight areas with suspicious features. Studies have shown that CAD systems improve the accuracy of diagnosis and increase the productivity of the human expert [24–27]. Figure 1.1 gives the flow diagram of a generic CAD system for lesion detection in the medical images. The first step is to segment the organ of interest from the original image. The next step is to identify possible regions within the segmented organ likely to be lesions. The next step further analyses these regions by segmenting the individual lesion candidates and collecting their pattern features. Finally, classification is carried out to determine whether the lesions candidates are really lesions or not.

The organ of interest in this study is the lung, segmented from a thoracic CT image. The purpose of lung segmentation is for accurate identification of the lung tissue and boundary [20] and to make the rest of the steps of the CAD focus on the lungs [23]. Lung segmentation is important because it reduces the computation time required in image analysis as the lungs occupy only a fraction of the CT image. It also ensures that all the parts of the lungs are considered for analysis

and included in the final result, as excluded areas of the lung which cannot be analyzed reduces the accuracy of the CAD system. Before the invention of CT, chest radiographs were used in diagnosis of disorders of the lungs. However, CT revolutionized thoracic imaging [28] by producing more detailed images than chest x-rays, and it has been shown to provide better diagnostic performance [29–31] due to the ease of detecting subtle changes in the lungs compared with using conventional chest radiography images.

The approach to lung segmentation used in this dissertation is to formulate the task of segmentation as a binary labeling problem and employ Graph Cut optimization technique to efficiently solve it. The goal of binary labeling is to partition the image into two classes by assigning labels to pixels in the original image. One of the labels is assigned to pixels belonging to lungs while the other label is assigned to pixels belonging to the chest structures and the background air surrounding the chest wall.

Graph Cut provides an efficient method of solving the binary labeling problem [32]. The information in the image is represented by modeling the image data and the spatial relationships existing between image pixels in an objective energy function. The global minimum of the energy corresponds to the optimal segmentation result [33].

1.2 Motivation

A method which accurately performs lung segmentation is the desired goal of this dissertation. Segmentation is an ill-posed problem and depends on certain criteria for grouping pixels, such as range of intensity values, gradient information or texture. The domain of application determines the criteria and characteristics used to group the pixels for a correct solution. This implies that there is still room for improvement of the existing methods of lung segmentation due to the availability of newer and more computationally efficient algorithms yielding potentially more accurate results than those previously used.

1.3 Problem Statement

The lungs are air-filled organs in the thoracic region of the human body. In a CT image, the lungs appear as dark regions while the structures such as the bones of the rib cage, muscles and blood vessels surrounding the lungs have intensity values ranging from from gray to white. An axial slice CT image is shown in Figure 1.2. For the purpose of subsequent discussions, three regions are identified from a typical CT slice namely, the lungs, the chest structures and the background surrounding the chest wall.

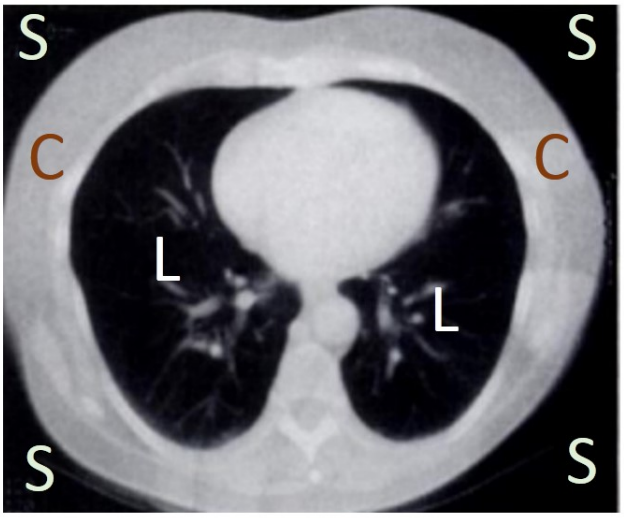

FIGURE 1.2: Axial CT slice of the thoracic region. The regions marked 'L' are the lungs. The region marked 'C' are the chest structures. The regions marked 'S' are the background surrounding the chest wall. Image from [34]

Several methods proposed in the literature for lung segmentation exploit the contrast between the dark lungs and the brighter surrounding structures and usually include a method for binary partitioning of the image usually performed with thresholding. It is expected that the method will partition the image into two classes with one class containing pixels of the lungs. However, certain conditions under which CT images are acquired preclude them from conforming to this expectation. CT images are prone to artifacts due to the high number of independent measurements recorded from different detectors [35]. As a result, distortions occur on the image where the attenuation value on the reconstructed

image is different from the value recorded by the detectors. This becomes a problem as the quality of the image is reduced and can result in misdiagnosis due to normal tissues appearing abnormal and vice versa. Another difficulty in segmentation of CT images lies in the fact that the range of pixel intensity values for different anatomical regions overlap. In the case of the thoracic CT image, the pixels of the lungs have similar intensity value with pixels of the air surrounding the chest wall, and the pixels of the chest structures have similar intensity with pixels of blood vessels and pathologies within the lungs and this results in misclassified pixels.

Other methods proposed involve the use of prior knowledge of the lung to perform segmentation. This prior knowledge could be acquired through training and classification [36]. However, the accuracy of the methods will rely on the number of training examples available and can be computationally expensive. The prior knowledge can also be acquired interactively by the user specifying pixels and regions belonging to different anatomical regions of the body [33]. The challenge lies in determining the level of interactivity needed to obtain accurate results, that is, the number of clicks needed to perform the segmentation and the number of clicks needed to modify the result of the segmentation [37]. The results are therefore subjective to the knowledge and experience level of the users. Automatic methods are, however, much more desirable than manual or semi-automatic method as the aim of CAD is to improve the results of diagnosis by highlighting potentially abnormal areas which could be missed out due to fatigue or observational oversight [25].

1.4 Research Objectives

The broad objective of this dissertation is to propose a method for performing accurate lung segmentation using Graph Cut. Graph Cut algorithm allows the incorporation of prior knowledge into its energy framework. Prior knowledge consisting of contextual information can be used to output the required

segmentation results. The energy is made up of functions which model the appearance of the image and the spatial interaction between pairs of connected pixels. Minimizing this energy produces global optimal solutions. This implies that all regions satisfying the criteria of belonging to the object of interest will be included in the segmentation result. The inclusion of a prior into the Graph Cut energy serves to constrain the solution space. The challenge is therefore to find a suitable prior to constrain the solution. One of the requirements for such a prior includes the ability to handle the changing shape of the lungs. Traversing down the lungs from the apex to the base, the appearance of the lungs varies. Another requirement is that acquiring and incorporating the prior information should not incur high computational costs. Specific objectives pursued in this dissertation, therefore, include the following:

1. Investigate different lung segmentation methods currently used in the literature
2. Identify a suitable prior to restrict the solution space of the segmentation result using Graph Cut
3. Model an automatic framework for lung segmentation using the identified prior with Graph Cut
4. Compare the proposed method with the state-of-the-art

1.5 Contributions of the Dissertation

The main contributions of this dissertation can be summarized as follows: the introduction of a novel energy constraint for Graph Cut energy and a novel segmentation algorithm for lung segmentation using Graph Cut. These contributions are given as follows:

- **A distance-constrained energy function:** The distance-constrained energy function consists of an additional term called a *distance term* which

penalizes pixels based on their euclidean distance from the object of interest. The conventional Graph Cut formulation contains two functions. One function attempts to model the appearance of the data by associating labels with the observed model while the other encourages coherence by giving connected neighboring pixels similar labels. However, the function responsible for modeling the appearance of the data is only effective in modeling the global appearance. If there are other segments having the same appearance model as the object of interest, then those segments are also included in the segmentation result. Therefore, the *distance term* ensures that labels are assigned only to the pixels of the region of interest notwithstanding the presence of regions with similar appearance model.

- **An automatic lung segmentation framework using Graph Cut:** The distance-constrained energy is applied to the problem of segmenting the lungs from a CT image. This framework extends the work of Boykov and Jolly [33] whose method is semi-automatic and produces unconstrained solutions. The proposed method is automatic as it does not require user input and is carried out in four steps. The first step detects the lungs from the image using Fuzzy c-Means to cluster the image, Connected Components labeling to identify the components in the image and a set of rules to identify the component belonging to the lungs. The second step involves creating *distance images* by a applying Distance Transform on binary images derived from the clustered images. The third step formulates the energy to be minimized with Graph Cut. The *distance images* provide the prior information about the distance of pixels from the object of interest and is used to compute the distance term. The region and boundary term are also computed, and the energy function consisting of three terms is minimized. The fourth step uses morphological area opening to correct misclassification of high intensity structures within the lung.

1.6 Organization of the Dissertation

The rest of this dissertation is organized as follows.

- Chapter 2 reviews the literature on lung segmentation and lays the foundation for the work done in this study
- Chapter 3 provides details on the distance constraint incorporated into the energy for accurate lung segmentation
- Chapter 4 provides details on the automatic lung segmentation method using the distance-constrained energy
- Chapter 5 concludes the dissertation and provides directions for future work

Chapter 2

Background and Related Works

2.1 Introduction

This dissertation focuses on the formulation of segmentation as a binary labeling problem where the goal is to find the optimal segment to which each pixel belongs. This problem is usually solved by optimization. Inspired by both the success of Graph Cut in image segmentation and the inclusion of additional constraint into its basic energy formulation, an automatic segmentation method using Graph Cut optimization is proposed that makes use of a distance-constrained energy. In this chapter, The anatomy of the lungs and the thoracic CT slice are briefly introduced, previous works done on segmenting the lung from CT image and a general summary of works related to our approach in terms of introducing constraints into the basic energy formulation for medical imaging segmentation are presented .

2.2 Lungs and CT

2.2.1 Anatomy of the Lungs

The lungs is a cone-shaped organ in the chest and is the site of gas exchange for air coming into and leaving the body. There are two lungs; one on the left and one on the right. The left lung is divided into the upper lobe and the lower lobe while the right lung is divided into the upper, middle and lower lobes. The trachea is the main air pathway allowing air in and out of the body. The trachea divides into two bronchus, one enters the left lung and the other enters the right lung. The bronchus divides into smaller branches called bronchi and moves deeper into the lung tissue. The bronchi further divide into smaller pathways called bronchioles which end in tiny air sacs called alveoli. The gas exchange occurs in these tiny sacs.

The region of the lungs where the bronchi enters the lungs is called the hilum. The space between the lungs is called the mediastinum and it houses the heart, blood vessels, bronchi, and trachea. The space for the heart is called the cardiac notch. Figures 2.1 and 2.2 show the positions of the structures of the lungs described above.

2.2.2 Lungs in Thoracic CT image

The thorax can be viewed from the axial view, the coronal view, or the sagittal view as shown in Figure 2.3. The images used in this study are from the axial view.

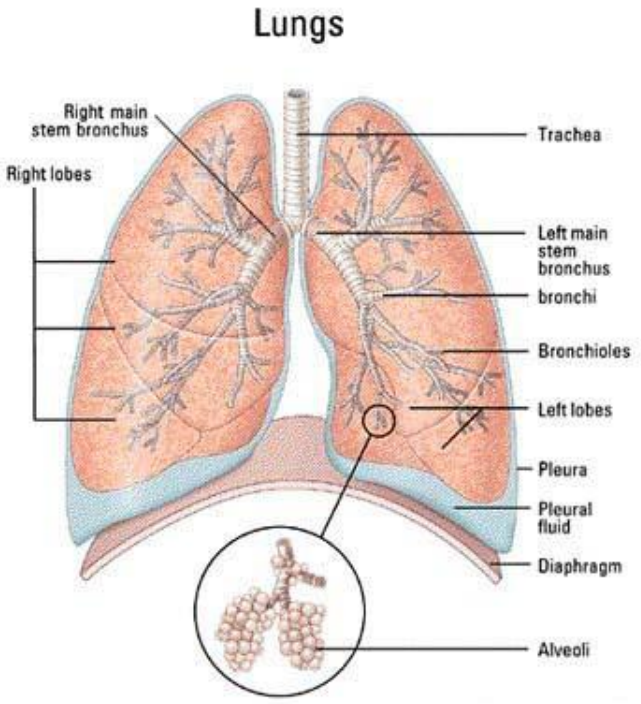

FIGURE 2.1: Lung anatomy showing the left and right lungs and the air pathways. From [38]

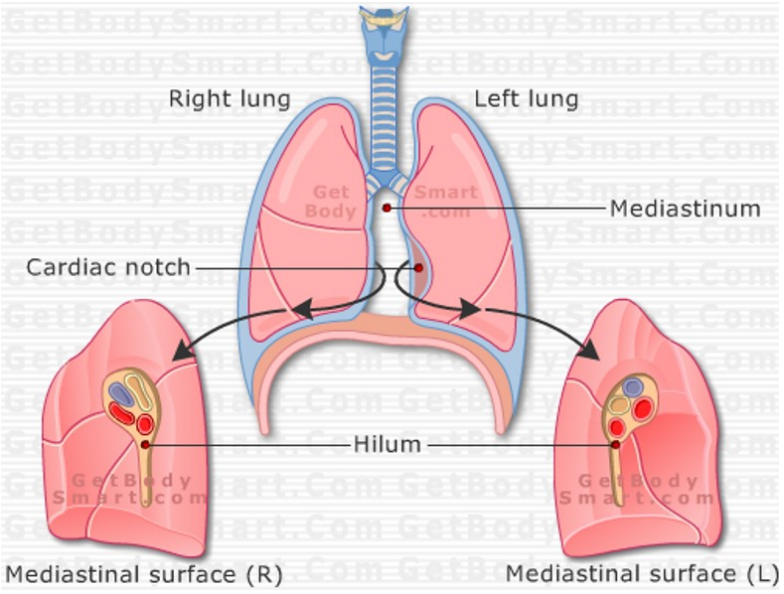

FIGURE 2.2: Lung anatomy showing the hilum, mediastinum and cardiac notch. From [39]

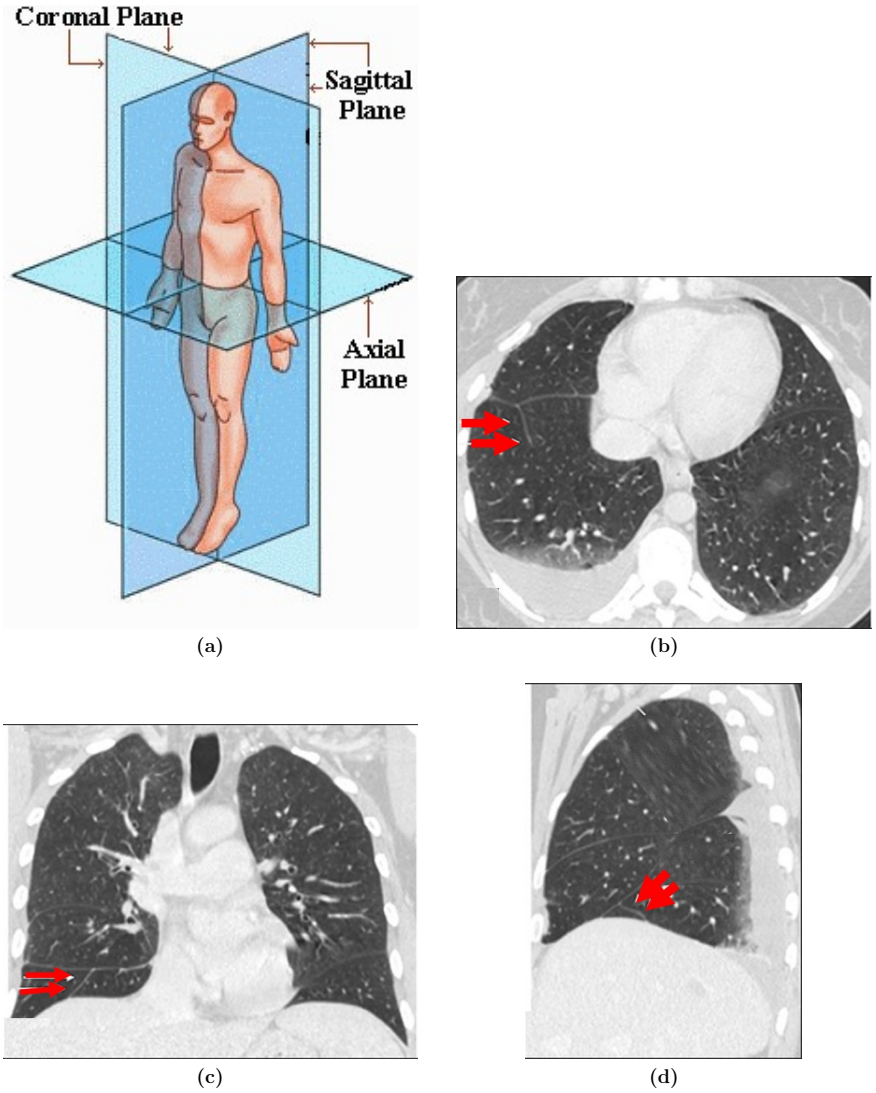

(a) (b) (c) (d)

FIGURE 2.3: Different viewing planes for a thoracic CT image (a) Planes of the body. From [40] (b) axial view (c) coronal view (d) sagittal view. Double arrows in (b), (c) and (d) show the location of the fissure in the three views. From [41]

2.3 Previous Lung Segmentation Methods on CT images

Given the contrast between the lungs and the surrounding chest structures in a CT image, segmenting the lungs has traditionally been solved as a binary partitioning problem with the pixels of the lung belonging to one class and the pixels of the surrounding chest structures belonging to another. Several methods [42–50] begin by initially partitioning the image into two classes with thresholding. Thresholding

finds an optmal value, called a threshold, such that pixel intensities below the threshold will be classified as lung pixels while pixel intensities above the threshold will be classified as background pixels. Using the notation shown in Figure 1.2, the lungs L, being air-filled organs, will have pixel intensity values similar to the air surrounding the chest wall S. Also, within L resides some high intensity structures such as blood vessels and possible pathological regions which have similar range of intensity values as C. This causes some pixels to be misclassified. Therefore, subsequent steps are necessary to correct this misclassification.

Hu et al. [42] used connected components labeling and topological analysis to distinguish the surrounding non-body air from the air within the lungs, followed by separation of the right and left lung, and a series of morphology operations including morphological closing, erosion and a variation of morphological opening to smooth the boundaries along the lung mediastinum where the major vessels and bronchi enter the lung. Antonelli et al. [43] used a method to first remove the air surrounding the chest wall before applying thresholding, thus eliminating the need to identify the lung pixels after thresholding. Subsequent steps include morphological opening and closing operations to enhance the borders, Sobel operator to identify the borders, thinning of the borders, lung border detection, border reconstruction and finally, filling of the lung cavities. Iqbal et al. [46] used a series of morphological operations to produce the final segmentation results. Mesanovic et al. [49] performs region growing after thresholding the image followed by edge detection and morphological operations to create a filled binary mask which is multiplied with the original image to separate the lung parenchyma from the image. Wei et al. [50] useds connected components labeling to eliminate the air surrounding the chest wall followed by region growing to remove the airway which may still be present after eliminating the background. Next, left and right lung separation is performed, if necessary. The final step uses Bresenham Algorithm to smooth the lung boundary based on an improved chain code.

In the event that thresholding fails to find the optimal threshold separating the image into two classes with one class belonging to the air pixels, it becomes

impossible to use the subsequent steps of the method. An illustration is provided in Figure 2.4 where the optimal threshold does not produce the expected result. This failure is due to the fact that thresholding heavily depends on the intensity distribution of the image and assumes that its histogram is bimodal, and thus finding the center between each peak provides the optimal threshold value.

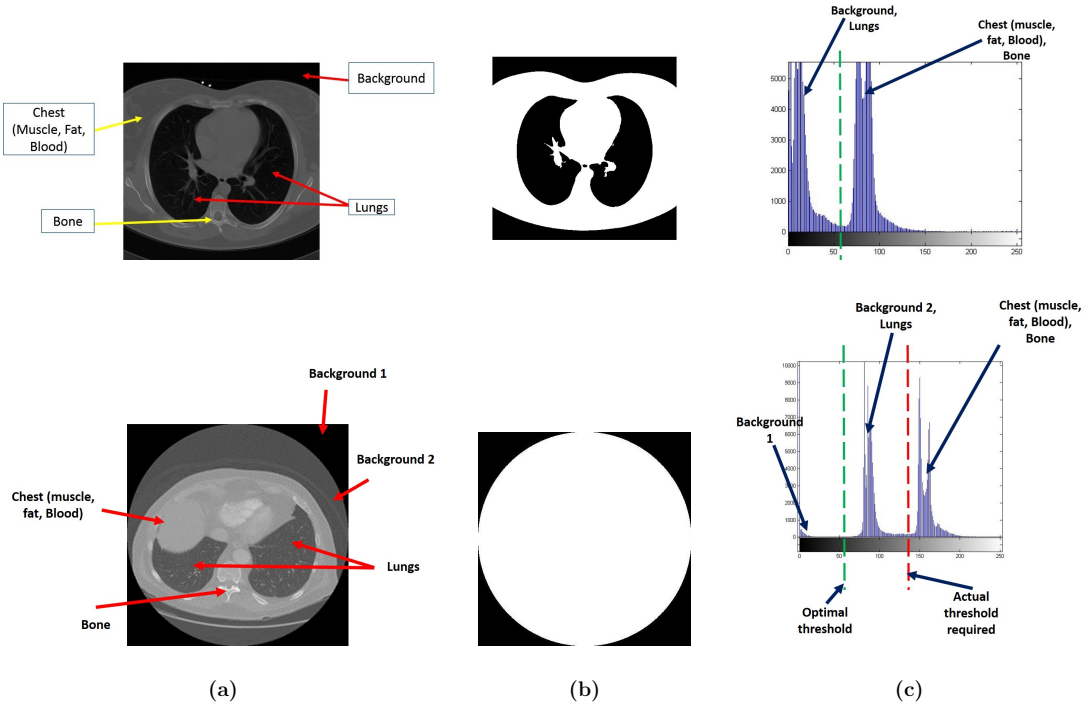

FIGURE 2.4: Comparison between a bimodal and trimodal histogram showing a scenario where thresholding fails. The green dotted line on the histogram in column (c) shows the threshold value selected by Otsu's [51] method. The red dotted line on the bottom histogram shows a possible threshold value which would have yielded the expected result

To reduce the dependency on thresholding, other methods such as [52–55] have been proposed. Shojaii et al. [52] proposed a method which segments the lung region by placing internal and external markers on a gradient image. Watershed transform is then used to find significant edges between the markers corresponding to the lung edges, and is followed by contour smoothing and filling of the area within the edges found by the transform. Abdollahi et al. [53] proposed a method consisting of four steps. In the first step, the Gaussian scale space of the image is created. The second step involves modeling the image data with Markov-Gibbs Random field (MGRF). The third step involves an initial

segmentation on all images in the scale space. The final step performs a fusion of the iterative refinement of the initial scale space segmentation to produce the final segmentation result. Kothavari and Deepa [55] used a robust active shape matching (RASM) model. The model is trained using the contours on manually delineated images done by experts. An initial contour is generated after training and is iteratively deformed to fit the shape of the lungs in the test images. The shape of the lungs varies depending on the part of the lung being examined, and depending on the position of the patient.

Reduced dependence on thresholding reduces the dependence on the pixel information to perform segmentation. Prior knowledge in the form of contextual information is incorporated within the method to get the required final result. In [52], knowledge of the range of intensity values for the anatomical objects in the CT image is required for correct placement of the internal and external markers. In [53], the assumption that the image can be modeled with an MGRF is the prior knowledge that is used for the data modeling step of the algorithm. In [55], manually delineated images provide the prior knowledge for the method.

The drawback of the reduced dependence is the increase in computational cost. The computational cost incurred using the method in [42] is far less expensive than the method in [55]. Therefore, accuracy and reproducibility of the results need to be balanced against computational costs.

2.4 Related Works

2.4.1 Binary Labeling and Graph Cut

Before presenting the related works, the binary labeling problem is defined and the solution with Graph Cut is shown. Many problems in Computer Vision are formulated as labeling problems. The goal of labeling is to assign values to objects based on observed data. To formally define the labeling problem, let Q represent the set of pixels $i = 1, 2, ..., n$ and L represent the set of k possible labels. The

labeling of Q over L is simply a function $f : Q \rightarrow L$ [56]. The labeling problem seeks to find the optimal labeling among a set of possible labels. For a problem with k labels and n pixels, the search space for the optimal labeling is of size k^n. As an example, consider the case of an image with 512×512 pixels with four labels to be assigned. The size of the search space is 262144^4. Thus, efficient algorithms are required to optimize the search for the optimal labeling.

There are two main groups of solutions proposed for optimization [57], namely, combinatorial optimization methods and linear programming methods. The problems solved by combinatorial optimization methods can be formulated as Maximum *A Posteriori* (MAP) inference problems [58] on discrete graphs and can be expressed as a MAP estimate of a Markov Random Field (MRF) [59, 60]. Combinatorial algorithms such as simulated annealing [59, 61] and Iterated Conditional Modes [60] were used to find the MAP estimate of the MRF. Greig et al. [32] showed that the solutions produced by the previous methods were far from the true labeling and proposed an exact optimization method for finding the MAP estimate in a binary labeling problem using the min-cut/max-flow theory [62]. This was the introduction of Graph Cut to computer vision and was first used in image restoration.

Boykov and Jolly [33] extended the Graph Cut method in [32] to image segmentation. Therefore, the MAP estimate refers to the segmented image and the binary labels L to be assigned are $L = \{\mathbf{O}, \mathbf{B}\}$ where $\mathbf{O}$ denotes pixels belonging to the object of interest and $\mathbf{B}$ denotes pixels belonging to the other regions generally referred to as the background. Let A be a binary vector that defines the segmentation. Therefore, for an image I with i number of pixels, the components of $A = (A_1, A_2, ..., A_i)$ specify the label L assigned to each pixel in I. Let N represent the set of all unordered pairs $\{i, j\}$ of neighboring elements in I derived from a standard neighborhood system e.g. 4-, 8- or 26- neighborhood system.

$$E(A) = \lambda \cdot R(A) + B(A) \tag{2.1}$$

where

$$R(A) = \sum_{i \in I} R_i(A_i) \tag{2.2}$$

$$B(A) = \sum_{\{i,j\} \in N} B_{i,j}.\delta_{A_i \neq A_j} \tag{2.3}$$

and

$$\delta_{A_i \neq A_j} = \begin{cases} 1, & \text{if} A_i \neq A_j \\ 0, & \text{if} A_i = A_j \end{cases}$$

$R(A)$ is called the regional term. It is the cost of assigning pixel i with either label **O** or **B** and is calculated as negative log-likelihoods for each pixel i with intensity q_i as shown in equation (2.4).

$$\begin{aligned} R_i(\mathbf{O}) &= -\ln \Pr(q_i|\mathbf{O}) \\ R_i(\mathbf{B}) &= -\ln \Pr(q_i|\mathbf{B}) \end{aligned} \tag{2.4}$$

The regional term is used to compute the cost for the edges connecting each pixel to the terminal nodes. These edges are called t-links. The higher the likelihood of a pixel belonging to **O**, the higher the cost on the t-link connecting the pixel to the source terminal and vice versa. Similarly, the higher the likelihood of a pixel belonging to **B**, the higher the cost on the t-link connecting the pixel to the sink terminal and vice versa.

$B(A)$ is called the boundary term. It is responsible for the smoothness of the boundary of the final segmentation and penalizes dissimilarities between neighboring pixels. It is calculated as shown in equation (2.5).

$$B_{i,j}(q_i, q_j) = \exp\left(\frac{(q_i - q_j)^2}{2\sigma^2}\right) \tag{2.5}$$

where q_i and q_j are neighboring pixels and σ can be estimated as "camera noise". The boundary term is used to compute the cost for the edges connecting neighborhood pixels. These edges are called n-links. The higher the similarity of intensity value of pixels pairs within the same neighborhood, the more likely they

are to be assigned the same label, thus the cost on the n-link will be higher and vice versa.

λ is used to determine the relative importance of the regional term to the boundary term. The contribution of each term in the energy function affects the final segmentation result, and λ is used to balance the contribution of each term. In literature, λ is usually determined experimentally.

Fig. 2.5 illustrates image segmentation with Graph Cut. The min-cut/max-flow algorithm [62] finds the minimum sum of edge costs (both t-links and n-links) on the graph such that when the edges contributing to the minimum costs are removed, the graph is partitioned into two classes; one class is labeled as the object of interest and the other is labeled as the background.

2.4.2 Incorporating Constraints into the Graph Cut Energy

In medical image segmentation, the objective is to segment the image into objects corresponding to anatomical parts of the body. In most cases, a specific body part is the region of interest for further study, and segmentation is used to extract this region from the image. Graph Cut produces globally optimal solutions which are topologically unrestrained [63] meaning that all regions with similar properties are assigned the same labels. This makes the segmentation of medical images difficult because pixel intensity values of the objects in the image overlap and, in some cases, boundaries separating the different objects are unclear. Therefore, using the function in equation (2.1) includes both the anatomical object of interest and other regions with similar properties to the object of interest in the segmentation result. The following studies show the incorporation of extra constraints in the energy function for segmentation of medical images.

Slabaugh and Unal [1] presented a method for segmentation using elliptical shape priors to reduce the effect of misleading cues such as weak boundaries and noise from the solution space. They used an iterative method which identifies an initial

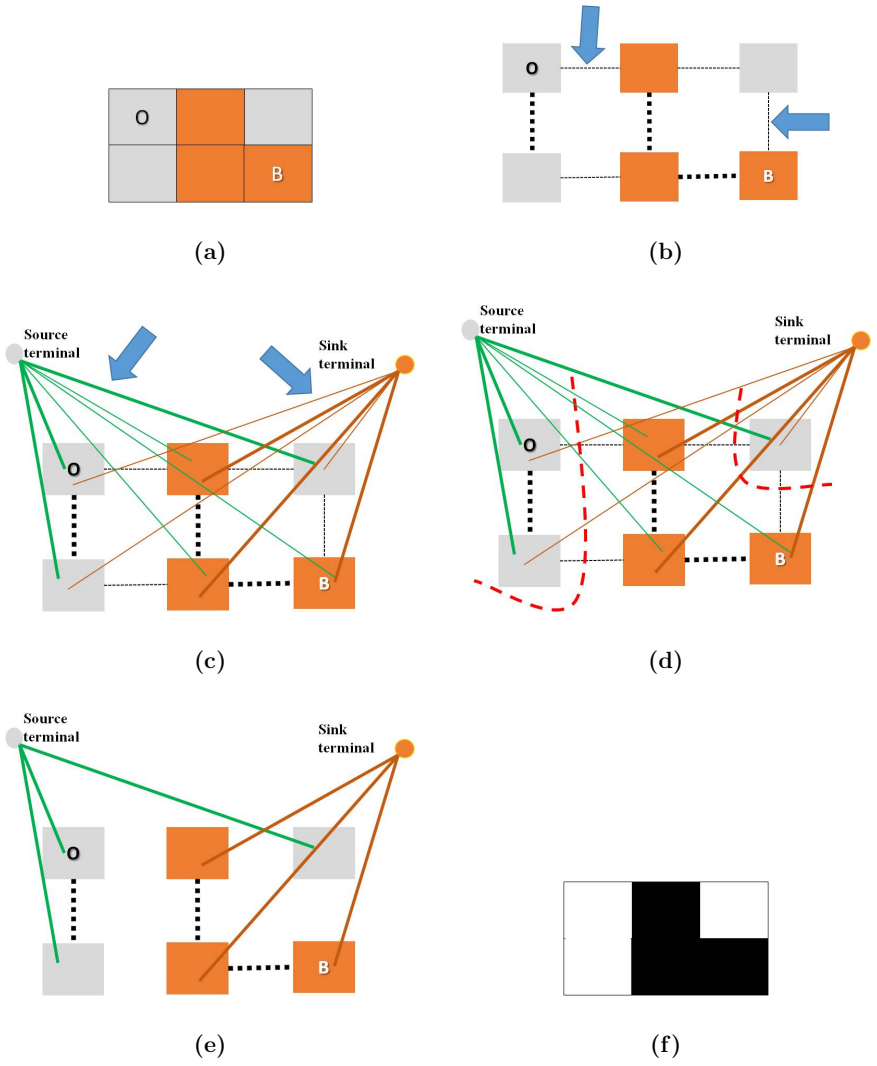

FIGURE 2.5: Image Segmentation using Graph Cut (a) Original Image (b) and (c) show the graph construction from the image. The edge weights are depicted by the thickness of the edges. In (b) the blue arrows show the n-links connecting neighborhood pixels. In (c) the t-links are included showing the pixels' connection to the source and sink terminals. (d) the cut on the graph is shown in red dotted lines (e) shows the removed edges (f) segmented image showing the pixels labeled as object and background

ellipse, constructs the graph within that ellipse in a narrow band and performs a minimum cut on the graph. The new ellipse formed by finding the best fitting ellipse to the points of the segmentation. A new narrow band is formed around the new ellipse and the methods iterates until convergence. Figure 2.6 provides the narrow band used in the method. The energy used for the segmentation is

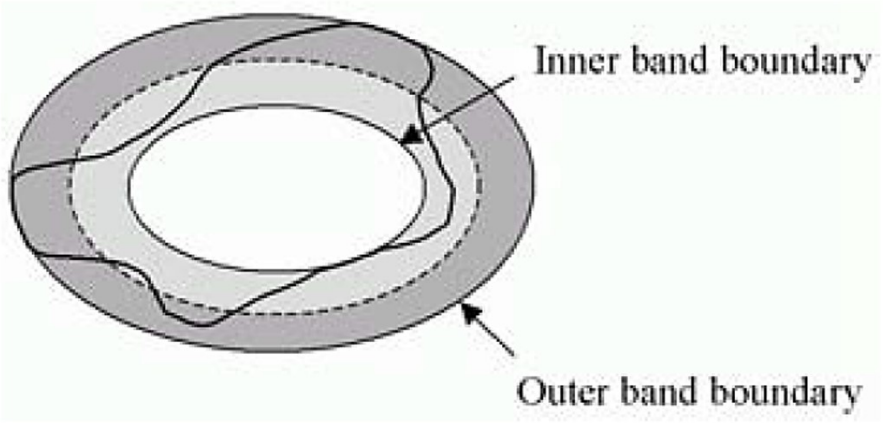

FIGURE 2.6: Narrow band containing the ellipse used in [1]. The minimum cut is shown as a dark contour

made up of two energy terms, and each of the energy terms is of the form

$$E(L) = \sum_{p \in \mathbf{P}} D_p(f_p) \; + \sum_{\{p,q\} \in \mathbf{N}} V_{p,q}(f_p, f_q) \tag{2.6}$$

where E is the energy, p and q are pixels, $\mathbf{N}$ is the neighborhood connectivity, $D_p(f_p)$ measures the cost of assigning the label f_p to p while $V_{p,q}(f_p, f_q)$ measures the cost of assigning labels f_p, f_q to neighboring pixels p, q.

The first energy term is the image-based energy term. Given an ellipse, the mean intensity of the pixels inside an outside the ellipse is u_i and u_o respectively. The energy is given as follows:

$$\begin{aligned} D_p(\text{foreground} &= |I(p) - u_i| \\ D_p(\text{background} &= |I(p) - u_o| \end{aligned} \tag{2.7}$$

and $V_{p,q}$ is the as described in [33].

The second energy term is the shape-based energy term. For the shape prior, a shape mask M is formed which is a binary image such that inside the ellipse is 0 and outside the ellipse is 1. The energy is given as follows:

$$\begin{aligned} D_p(\text{foreground} &= |M(p) - 1| \\ D_p(\text{background} &= |M(p) - 0| \end{aligned} \tag{2.8}$$

and $V_{p,q}$ is the as described in [33]. λ measures the contribution of the shape term.

Figure 2.7 provides an example of the results of the elliptical prior.

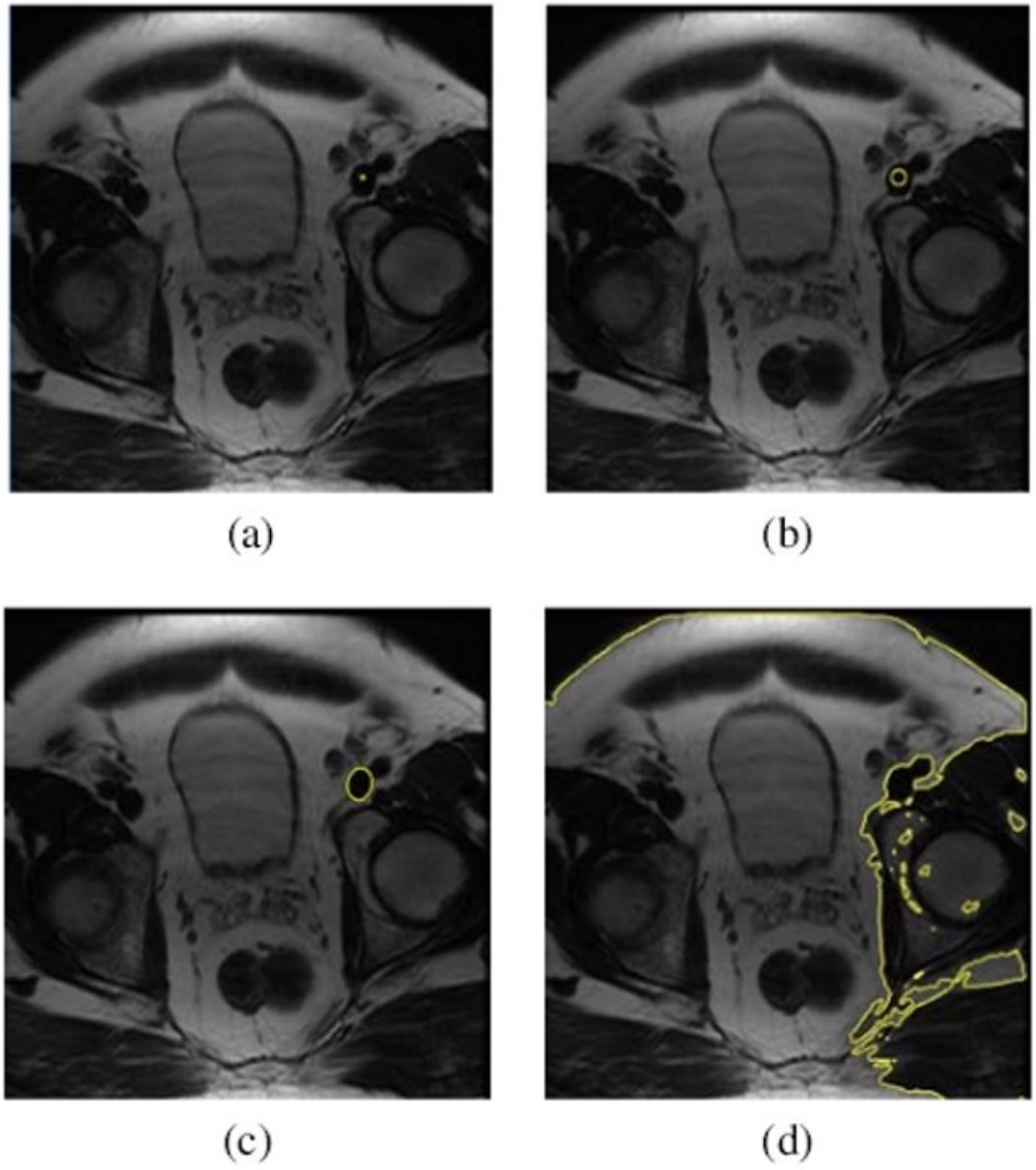

FIGURE 2.7: An example showing the results of elliptical prior used by Slabaugh and Unal to find a blood vessel in a pelvic MRI image. (a) shows the user clicks yellow (b) shows the evolution of the ellipse until (c) where it achieves the segmentation. (d) shows the result of the segmentation without the elliptical prior. Graph Cut included all the regions which had the same pixel characteristics as the region of interest

Funka-Lea et al. [2] added a blob prior to prevent the inclusion of surrounding organs from the solution when segmenting the outer surface of the heart from a

cardiac CT scan. The function is given as

$$E(f) = E_{smooth}(f) + E_{data}(f) + E_{blob}(f) \tag{2.9}$$

$E_{smooth}(f)$ and $E_{data}(f)$ are given as

$$\begin{aligned} E_{data}(f) &= \sum_{p \in \mathbf{P}} D_p(f_p) \\ E_{smooth}(f) &= \sum_{\{p,q\} \in \mathbf{N}} V_{p,q}(f_p, f_q) \end{aligned} \tag{2.10}$$

where $D_p(f_p)$ is the likelihood function of label f_p for a given pixel p and $V_{p,q}$ is the interaction function between pixels {p,q} in a neighborhood given a neighborhood system $\mathbf{N}$.

An energy consisting of only $E_{smooth}(f)$ and $E_{data}(f)$ is the basic formulation for Graph Cut. $E_{smooth}(f)$ imposes the smoothness constraint on the segmentation result while $E_{data}(f)$ measures how well the label f fits with the data. $E_{blob}(f)$ in equation (2.9) is the extra constraint included in the energy and is given as

$$E_{blob}(f) = \sum_{\{p,q\} \in \mathbf{N}} B_{p,q}(f_p, f_q; C) \tag{2.11}$$

where C is the center of the seed-region and $B_{p,q}$ is a Potts interaction model which penalizes discontinuity depending on the angle between line segments pq and pC. Therefore,

$$B_{p,q}(f_p, f_q) = \begin{cases} (pq, pC) * T(f_p \neq f_q), & \text{if } (pq, pC) < 0 \\ 0, & \text{else} \end{cases}$$

The introduction of the blob prior makes the cuts produced by the energy function to appear as a convex blob.

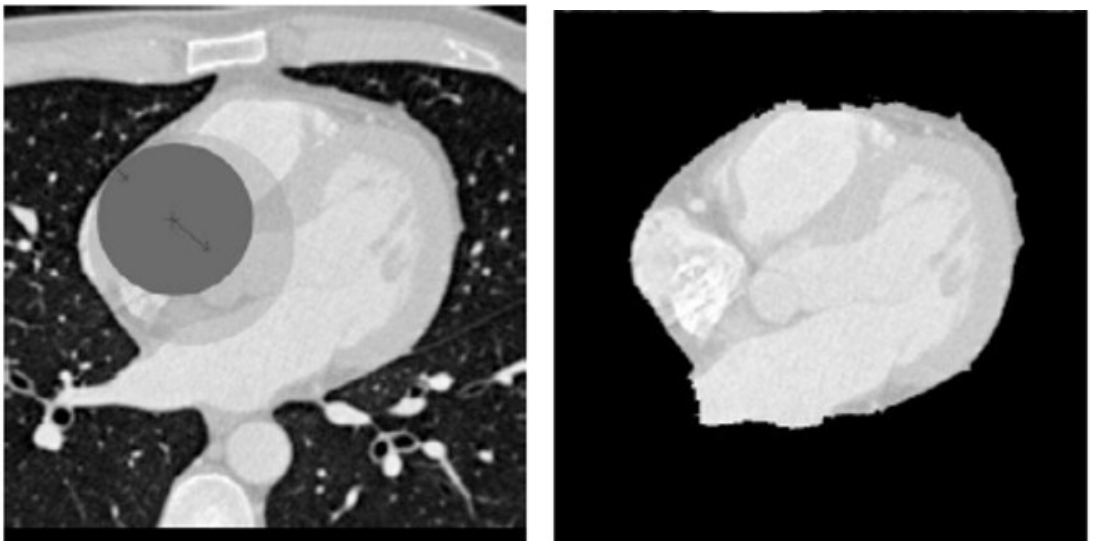

(a) (b)

FIGURE 2.8: An example showing the results of blob prior used by Funka-Lea et al. [2] to segment the heart. (a) shows the initial "balloon" expanded within heart (b) The heart segmented out of the image appearing as a convex blob

2.5 Conclusion

The dependence on thresholding for initial binary partitioning of the image may lead to inconsistent results. Several successful methods have been proposed which reduce or totally eliminate the need for thresholding. However, there is an accompanying increase in computational cost, especially in those methods which include training a model or a shape prior.

The success of Graph Cut in image segmentation is the motivation for its use in this study. However, the general formulation of the energy function does not allow the accurate isolation of a single body part due to the fact that, in medical images, the range of pixel intensity for different anatomical regions tend to overlap, and graph cut produces globally optimal solutions. This, therefore, implies that all the regions which have the same range of intensity as the body part of interest will be included in the final result.

Several energy formulations have been proposed which incorporate an additional constraint to reduce the solution space, thereby producing the required segmentation result. However, the solutions proposed have some characteristics

in common which might limit their success in lung segmentation. Firstly, the anatomy of interest usually has approximately the same shape across a variety of images. Secondly, only one connected region or anatomy is usually sought. In the case of the lungs, its shape changes moving from the apex to the base of the lung. Therefore, a flexible prior which takes into account the changing shape of the lungs is needed to segment the lungs from the image. In the axial CT slice, two unconnected regions of different shape and size are the required output of the segmentation.

Finally, most implementations of Graph Cut are semi-automatic or interactive in nature. They involve the user selecting certain pixels, called seeds, to belonging the object of interest and the background. While, this provides certain control over the results, there is a lack of control over how many seeds are required for each image, and the best location to place the seeds to get the best results.

The next chapter introduces the distance prior proposed as the additional constraint on the solution space. Several experiments are carried out which demonstrate its suitability in producing accurate lung segmentation results.

Chapter 3

The Distance-Constrained Energy (DCE) function

3.1 Introduction

Graph Cut optimization is a technique used to find the optimal segment. The optimal solution determined by Graph Cut is dependent on the energy function used to define the segmentation problem [33]. In this chapter, a distance-constrained energy function is presented for lung segmentation.

The distance prior is introduced in section 3.2 and the distance-constrained energy incorporating the distance prior will also be described. The experimental setup and results demonstrating the suitability of the distance prior in constraining the segmentation solution will be discussed in sections 3.3 and 3.4 respectively.

3.2 Distance Prior

A distance prior is proposed as the additional constraint in the energy function using Graph Cut to accurately segment the lungs from the CT image. The distance refers to the Euclidean distance between pixels. Specifically, a distance term $K(A)$

is incorporated into equation (2.1) to provide the extra constraint. The distance term can be estimated from *distance images* which is discussed in detail in Section 4.2.2. The new equation will be referred to as the *distance-constrained energy (DCE)* and is given in equation (3.1).

$$E(A) = \lambda \sum_{i \in \mathbf{I}} R(A) \; + \sum_{\{i,j\} \in \mathbf{N}} B(A) \; + \sum_{i \in \mathbf{I}} K(A) \tag{3.1}$$

The distance constraint, therefore, assigns weight on the T-links as follows:

$$K_i(q_i \in \mathbf{O} | dist_i < Th_o) = \begin{cases} \infty, & \text{for } S_i \\ 0, & \text{for } T_i \end{cases} \tag{3.2}$$

$$K_i(dist_i > Th_b) = \begin{cases} 0, & \text{for } S_i \\ \infty, & \text{for } T_i \end{cases} \tag{3.3}$$

where $dist_i$ is the distance of pixel i and Th_o and Th_b are thresholds on the distance, S_i and and T_i are the source and sink terminal links for the pixels satisfying the conditions $(q_i \in \mathbf{O} | dist_i < Th_o)$ and $(dist_i > Th_b)$. The condition in equation 3.3 does not specify whether the pixel belongs to **O** or **B** and thus affects any pixel at a distance greater than the specified threshold Th_b. Figure 3.1 illustrates the weight placement on the graph and shows the final result. Pixel 3 has been assigned ∞ on the source T-link and has no sink T-link ($\equiv 0$). All the pixels apart from pixel 3 have been given an ∞ weight on the sink T-links and no weight ($\equiv 0$) on the source T-links. This ensures that pixel 3 is given a different label from pixel 1 and 2. This forces only the N-links and T-links connecting pixel 3 to be cut (shown in Figure 3.1(c)) and labeled differently from the other object pixels (shown in Figure 3.1(d)).

In equation (2.1), R(A) determines the weight on the T-links. However, in equation (3.1), both R(A) and K(A) are responsible for weighting the T-links. Only the weight on the T-links are being reweighed because the boundary term is sufficient

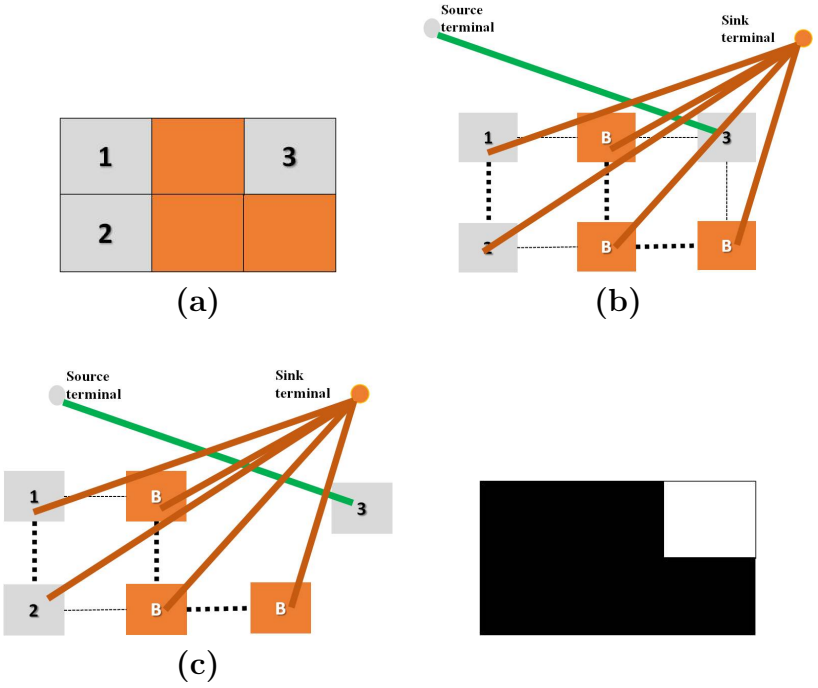

FIGURE 3.1: (a) Original Image (b) Graph showing the edge weight (note the thickness of each T-link) (c) Edges cut from the Graph (note the edges around pixel 3) (d) Segmented image

enough to produce smooth boundaries in the final segmentation. The regional term, however, is not sufficient to correctly isolate the lungs from the image due to the presence of air surrounding the chest cavity which have intensity values similar to the lungs. Since the regional term controls the weights on the T-links, any modification will be done on the T-links. This is why the distance term has been introduced; to assist the regional term. Figure 3.2 provides an illustration of the regions which the conditions for the distance term operate upon in a lung CT image. In Figure 3.2(b), any pixel within the shaded region having pixel intensity similar to the object of interest is given an ∞ weight on the source T-links and 0 on the sink T-links. In Figure 3.2(c), any pixel within the shaded region is assigned an ∞ weight on the sink T-links and 0 on the source T-links. The borders of the shaded regions represent the distance thresholds Th_o and Th_b.

Therefore, any pixel which does not satisfy either condition in the distance term is weighted by the regional term. The procedure for weighting the T-links using both R(A) and K(A) is given in Algorithm 1

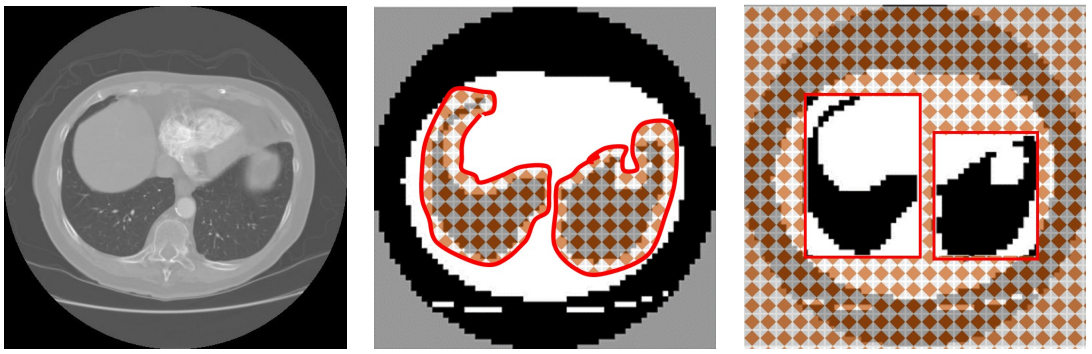

(a) (b)

FIGURE 3.2: Illustration of the regions upon which the distance term operates. The image is a CT scan which has been clustered into three classes. (a) Original Image (b) Shaded region $dist_i < Th_o$ within which the object pixels are searched for (c) Shaded region $dist_i > Th_b$

Algorithm 1 Computing the weights on the t-links for the DCE

if $i \in \mathbf{O}$ and $dist_i < Th_o$ **then**
  $S_i = \infty$
  $T_i = 0$
else if $p \in \mathbf{B}$ and $dist_i > Th_b$ **then**
  $S_i = 0$
  $T_i = \infty$
else
  $S_i = -\lambda \ln \Pr(q_i|\mathbf{B})$
  $T_i = -\lambda \ln \Pr(q_i|\mathbf{O})$
end if

3.3 Experimental Setup

In this section, the results of using the distance prior for segmentation is evaluated. The image data used in the experiments are first described and then the experimental results are presented.

3.3.1 Image Data

The images were randomly selected from two publicly available databases namely: the Lung Image Database Consortium and Image Database Resource Initiative (LIDC-IDRI) and Lung Test Images from Motol Environment (Lung TIME). A total of 100 images were used in the experiments.

1. LIDC-IDRI: The LIDC-IDRI database [64] was a project initiated by the National Cancer Institute (NCI), further advanced by the Foundation for the National Institutes of Health (FNIH), and accompanied by the Food and Drug Administration (FDA). The database consists of 1018 cases of diagnostic and lung cancer screening thoracic CT scans with annotated lesions taken from different scanners supplied by different vendors. Each slice has a size of 512 × 512 pixels stored in DICOM format

2. Lung Test Images from Motol Environment (Lung TIME): Lung TIME database [65] was made in cooperation with the Centre of Machine Perception of Czech University, Prague and department of Imaging Methods of Motol Hospital in Prague. The dataset consists of two parts. The first part (TIME1) contains data from adolescent patients with 148 scans, 5mm slice thickness and 1mm slice spacing. The second dataset (TIME2) contains 9 scans with 5mm thickness and 5mm slice spacing. The images are stored in DICOM 3.0 format and have a size of 512 × 512 pixels.

3.3.2 Performance Metrics

Sensitivity, Specificity and Accuracy [66] are the metrics used to measure the performance of the distance prior in segmenting the lungs.

$$Sensitivity = \frac{TP}{TP + FN} \tag{3.4}$$

$$Specificity = \frac{TN}{TN + FP} \tag{3.5}$$

$$Accuracy = \frac{TP + TN}{TP + TN + FP + FN} \tag{3.6}$$

where TP is the number of pixels correctly labeled as lung pixels, FP is the number of pixels incorrectly labeled as lung pixels, FN is the number of pixels incorrectly labeled as non-lung pixels, and TN is the number of pixels correctly labeled as non-lung pixels.

Sensitivity measures the ability of the algorithm to correctly identify the lung pixels. Specificity measures to the ability of the algorithm to correctly identify the non-lung pixels. Accuracy measures the ability of the method to isolate the lungs from the image. The performance indices for the three metrics range from zero to one, with an index of zero signifying poor performance and an index of one signifying high performance.

3.4 Experimental Results

To validate the distance prior, the segmentation results using the DCE are compared with the segmentation results using the energy in Boykov and Jolly's Graph Cut algorithm [33] to show the improvements made by the use of the distance prior in the segmentation results. The experiments were implemented in MATLAB® R2010a using its Image Processing toolbox on a system with Intel Core(TM) i7-4770S @ 3.10Ghz, 8.00GB RAM. The max-flow algorithm by Boykov and Kolmogorov [67] is used for energy minimization.

The results of the comparison are presented in Tables 3.1, 3.2, 3.3 and Figure 3.3. The distance prior increases the sensitivity of the results slightly but improves the specificity and accuracy of the results tremendously. Without the distance prior, the specificity is low because the background surrounding the chest wall is incorrectly labeled as part of the lungs, and this in turn reduces the Accuracy of the segmentation.

The visual segmentation results for images from LIDC, TIME1 and TIME2 are presented in Figures 3.4, 3.5 and 3.6 respectively. Segmentation with distance prior is successful in separating the lung pixels from pixels with similar intensity

values surrounding the chest walls compared to the segmentation without distance prior which includes the background air surrounding the chest wall.

Table 3.1: Quantitative Comparison of the LIDC-IDRI segmentation results with and without distance prior

	Without DP	With DP
Sensitivity	0.9659	0.9978
Specificity	0.4155	0.9944
Accuracy	0.4776	0.9953

Table 3.2: Quantitative Comparison of the TIME1 segmentation results with and without distance prior

	Without DP	With DP
Sensitivity	0.9542	0.9865
Specificity	0.7040	0.9999
Accuracy	0.7834	0.9957

Table 3.3: Quantitative Comparison of the TIME2 segmentation results with and without distance prior

	Without DP	With DP
Sensitivity	0.9333	0.9792
Specificity	0.5801	0.9991
Accuracy	0.6369	0.9959

3.5 Conclusion

In this chapter, the nature of Graph Cut has been discussed including its formulation as a binary labeling problem and the globally optimal solutions it produces. Due to the nature of the CT images, a distance prior, which penalizes pixels based on their euclidean distance to the lung region, has been introduced as an extra constraint in the energy framework to ensure that only the pixels belonging to the lungs are labeled as such. The segmentation results using the distance prior have been compared to segmentation results without the distance prior to show the improvements made to the results with the introduction of the distance prior.

In the next chapter, an automated segmentation method which utilizes the distance-constrained energy will be presented. The various steps necessary for a more robust segmentation method are discussed in detail. The experiments carried out will be presented and the experimental results obtained will be discussed.

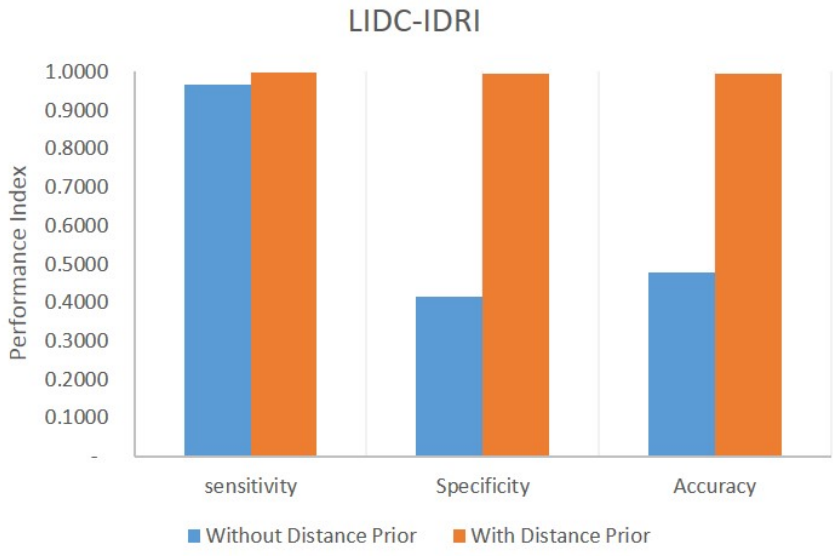

(a)

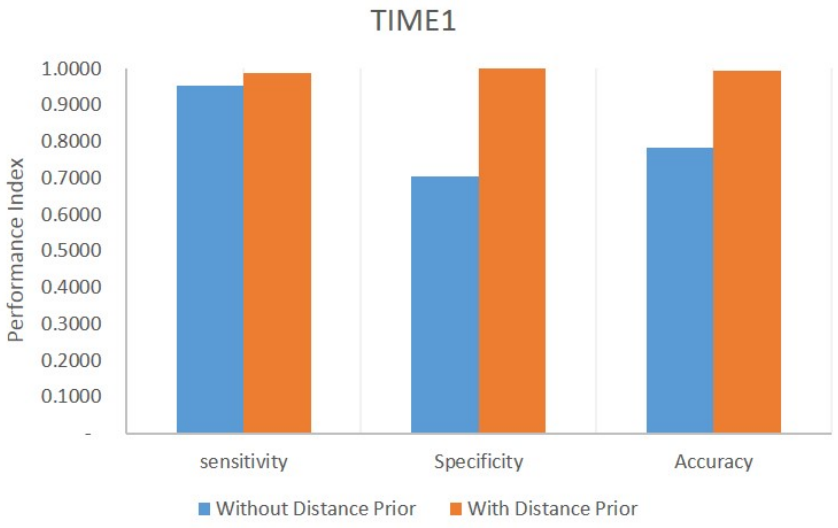

(b)

(c)

FIGURE 3.3: Graphical Comparison of the Sensitivity, Specificity and Accuracy of the segmentation results with and without the distance prior (a) LIDC-IDRI (b) TIME1 (c) TIME2

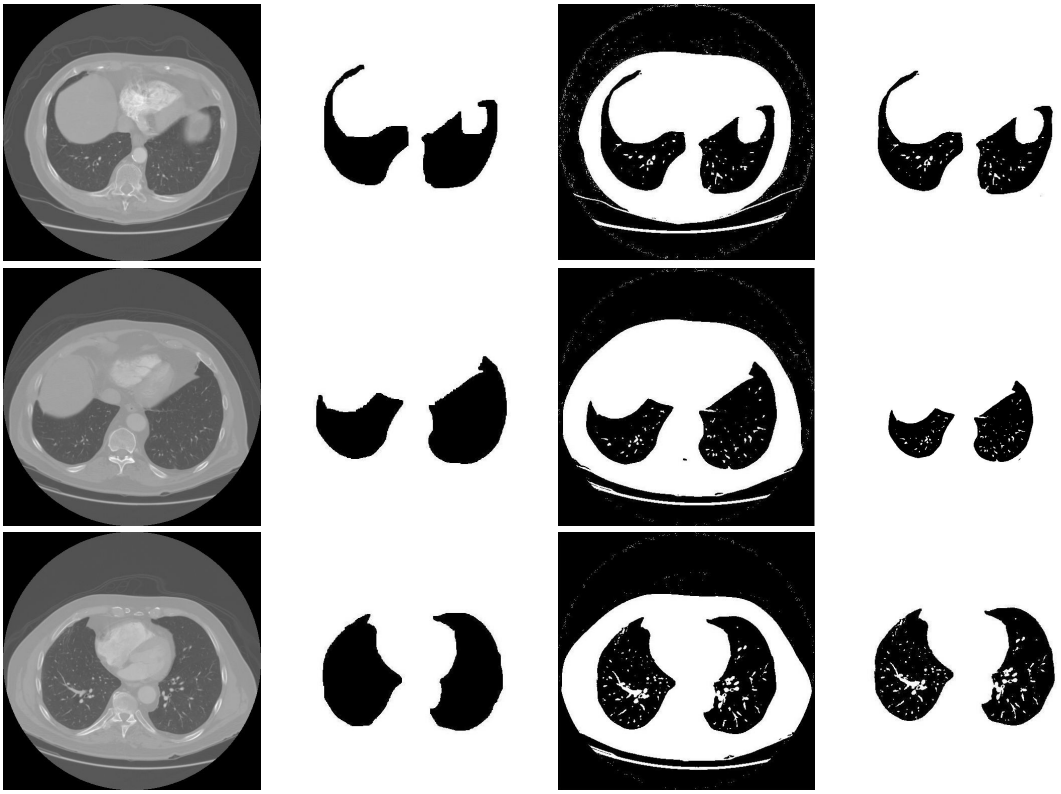

(a) (b) (c) (d)

FIGURE 3.4: Comparison of segmentation results using images from the LIDC database (a) Original Image (b) Ground Truth (c) Segmentation result without distance Prior (d) Segmentation with distance prior

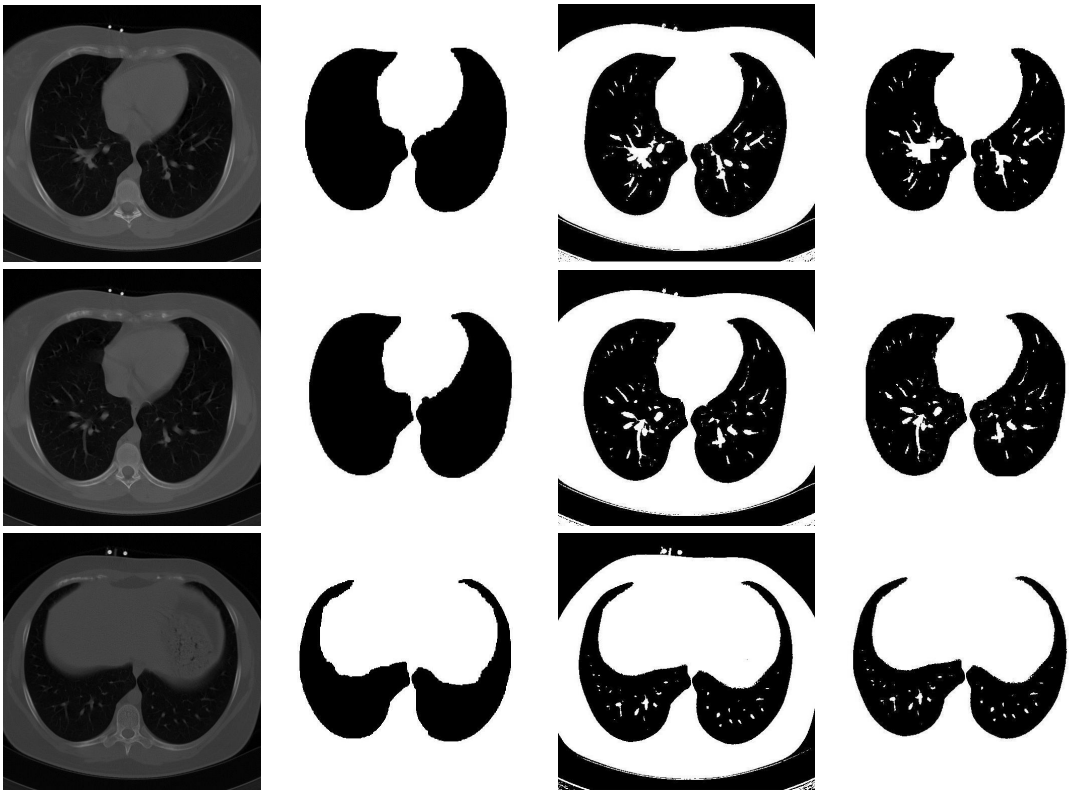

(a) (b) (c) (d)

FIGURE 3.5: Comparison of segmentation results using images from TIME1 database (a) Original Image (b) Ground Truth (c) Segmentation result without distance Prior (d) Segmentation with distance prior

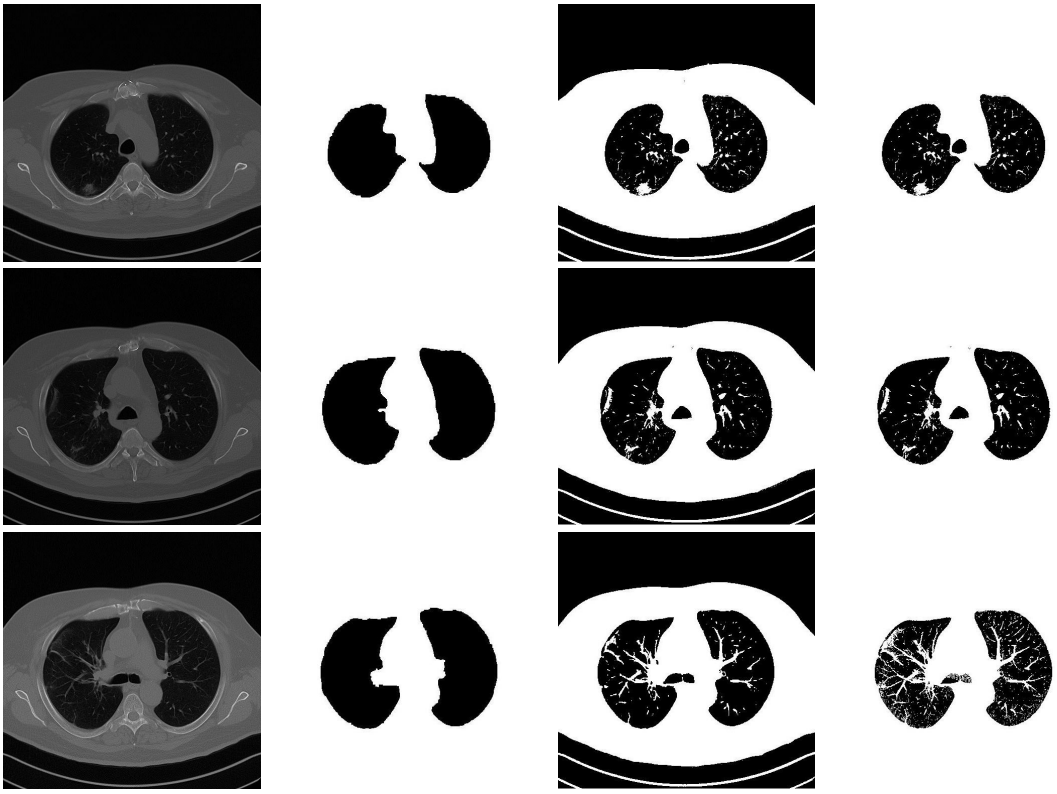

(a) (b) (c) (d)

FIGURE 3.6: Comparison of segmentation results using images from the TIME2 database (a) Original Image (b) Ground Truth (c) Segmentation result without distance Prior (d) Segmentation with distance prior

Chapter 4

Automatic Lung Segmentation

4.1 Introduction

Although segmentation results are influenced by the choice of energy function used, several other algorithms are often necessary for a robust performance of a segmentation method. In this chapter, the novel method for automatic lung segmentation using Graph Cut optimization, comprising of algorithms for lung region detection, calculation of the distances used for the distance prior, energy minimization and post-processing to correct mislabeled lung pixels, is presented.

Section 4.2 presents the overview of the proposed method and describes each step in detail. Section 4.3 provides the experimental setup including the image data, evaluation metrics and the experimental parameters used for performance evaluation. The experimental results are presented and discussed in section 4.4

4.2 Overview of the Proposed Method

The flow of the proposed segmentation method is shown in Figure 4.1. The first step involves splitting the image into non-overlapping blocks. The purpose of splitting the image is to reduce the effects of artifacts and stabilize the output

of the clustering, which is the next step after image splitting. It also has the advantage of reducing the runtime of the algorithm as instead of dealing with the pixels of the whole image, only a subset of pixels are used to represent the pixels within the each block of the image. After splitting the image, the mean of the pixels in each block are clustered into three classes. This is used to pre-label the image to get an initial estimate of the locations of the objects in the image.

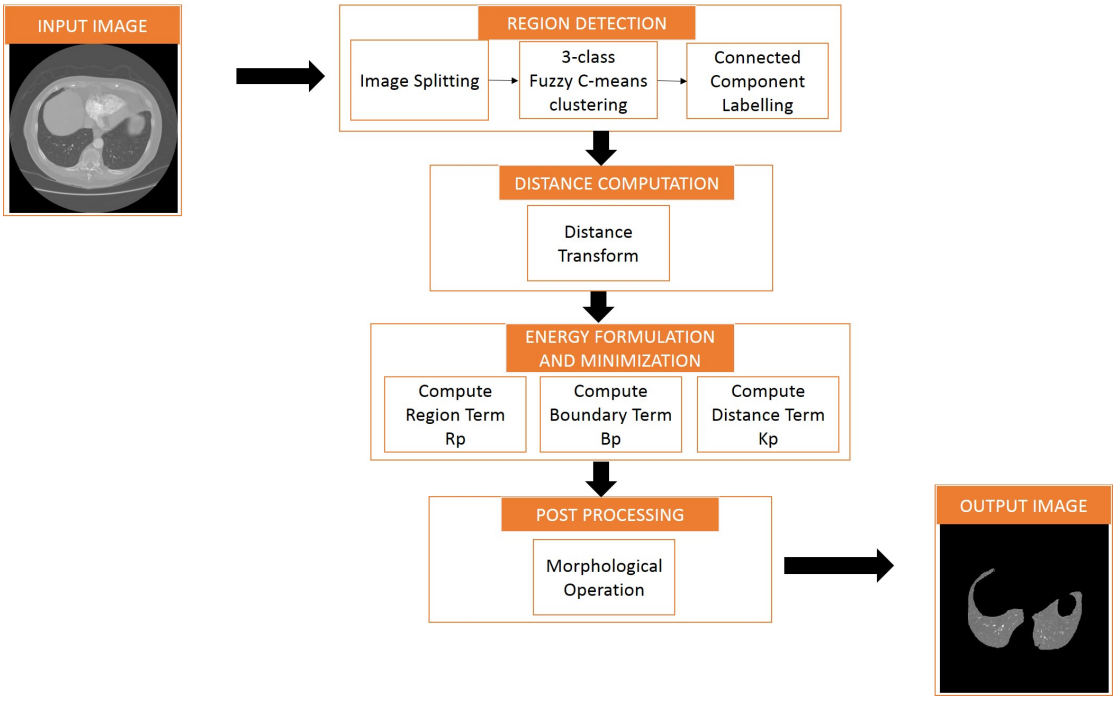

FIGURE 4.1: Proposed Method for Lung Segmentation

As the ultimate aim of binary segmentation is to partition the image into two, the logical step is to cluster the image into two classes. However, it has been found that binary partitioning does not always produce the desired result on some images [68]. Another observation made was that a 2-class FCM yielded unstable results due to the fact that FCM is sensitive to initialization. Using 3-class FCM provided stable results and for every time it was used, the results were always consistent.

Connected Components labeling is used to label the identified objects in the image after clustering. The bounding box surrounding each component and their respective areas are calculated. The aim of splitting, clustering and labeling the identified components in an image is to detect the lung components. This is

determined using the width to height ratio, the size of the components, and the proximity of the components to each other. The output of the lung region detection stage is an image with the bounding box delineating the detected lung components.

This is followed by computing the distances of pixels from the detected lung region. For this step, two binary images are derived from the output of the lung detection stage and two *distance images* are created by applying the distance transform on each image. The created images are referred to as *object distance images* and *background distance images*. The distance images provide the distance prior information to be incorporated into the energy framework of Graph Cut.

The final lung segmentation is done with Graph Cut making use of the DCE described in Chapter 3. The energy, formulated by computing the region term, the boundary term and the distance term, is minimized to yield the binary image where one class belongs to the lungs and the other class belongs to the chest structures and background surrounding the chest wall. There are some structures within the lungs which should be assigned the same label as the lungs, however, they have pixels with high intensity values similar to the chest structures, and thus, are assigned the same label as the chest structures. To correct this mislabeling, morphological area opening is used to assign the lung label to the structures within the lungs.

4.2.1 Region Detection

The lung detection process described in [68] is used for region detection. Let I represent the original CT image containing $M \times N$ pixels. The image is split into $M/p \times N/q$ non-overlapping blocks of size $p \times q$. Let $b_{k,l}$ be the $(k,l)^{th}$ block. The mean $\bar{b}_{k,l}$ of this block is calculated as

$$\bar{b}_{k,l} = \frac{1}{p \times q} \sum_{i=0}^{p-1} \sum_{j=0}^{q-1} I_{(i+p\times k),\ (j+q\times l)} \tag{4.1}$$

Let J represent the dataset containing $\bar{b}_{k,l}$. Each element $j_{k,l} \in J$ is the mean of $b_{k,l}$. The size of J is $M/p \times N/q$. FCM is run on J to partition it into three classes. The resulting clustered image is also of size $M/p \times N/q$.

To restore the clustered image back to the size of the original image, let C represent the clustered image of J with element $c_{k,l}$. The value of $c_{k,l}$ represents the class that $\bar{b}_{k,l}$ belongs to. Therefore, $c_{k,l}$ will be assigned to all the pixels in the $(k,l)^{th}$ block of the original image. Fig 4.2 provides an example of how the original image is split, clustered and restored back its original size

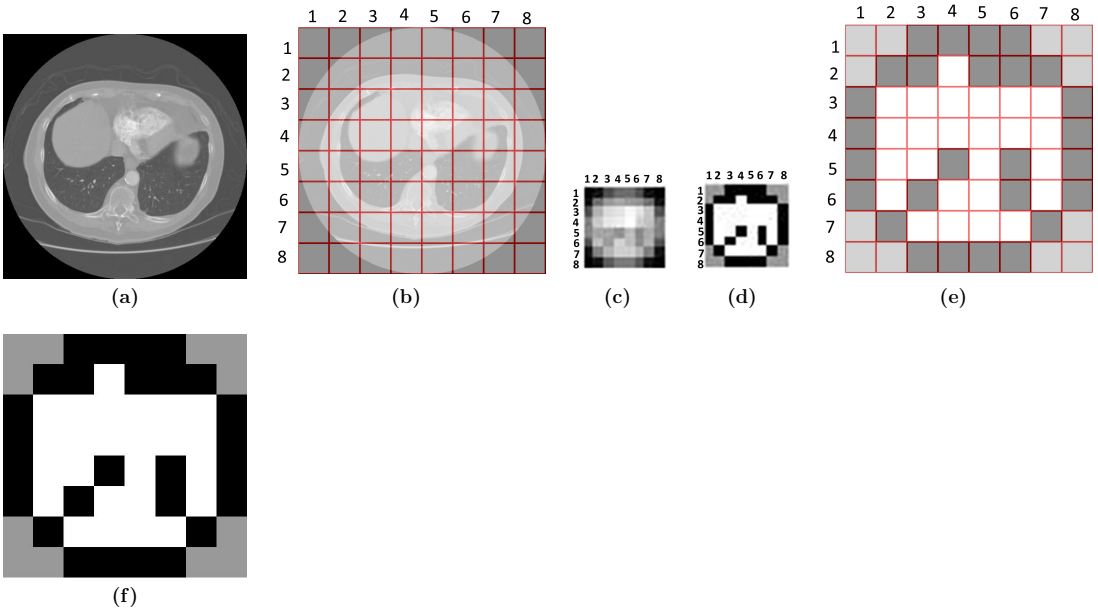

FIGURE 4.2: Example of an image of size 512×512 split into non-overlapping blocks of size 64×64 which reduces the image to a size of 8×8(a) Original image (b) Image split into non-overlapping blocks $b_{k,l}$ (c) J containing the mean of each block $\bar{b}_{k,l}$ (enlarged for clarity) (d) C the clustered image of J (enlarged for clarity) (e) The class membership of each $c_{k,l}$ in the C is transfered to the pixels in $b_{k,l}$. Each value in the matrix corresponds to one block of pixels in the image (f) Clustered image restored to the same size as the original image

Connected components labeling with 8-neighborhood connectivity is used to identify and label components in the clustered image. Figure 4.3 shows the identified components.

Properties such as the bounding box, area and size of each identified component are calculated. To identify the lungs, the size of the components and the width to height ratio of the bounding box are used. The rationale for these criteria is that

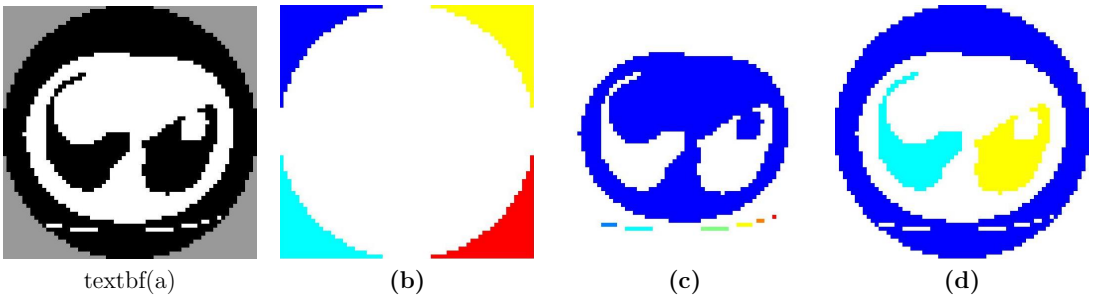

FIGURE 4.3: Connected Component labeling (a) Clustered Image. (b) - (d) shows the identified components for each partition. All the identified components are shown in different colors. The white colored areas are not part of the components.

the ratio of the width to height of the lungs is usually < 1 in most CT images and they are usually larger in size compared to other components whose ratios are also < 1. Other criteria was used in cases where the lung shape did not meet the ratio and area criteria. These include identifying components with relatively comparable sizes and determining whether they belong to the same class. The rationale is that the area of the two lungs in a CT image are usually close in size. Therefore, two components with similar area size and belonging to the same cluster have a high probability of being the lung components.

Figure 4.4 provides a summary of the region detection step.

FIGURE 4.4: Figure showing the steps of region detection (a) Original image (b) Image split into non-overlapping blocks (c) Clustered image (e) Detected lung component surrounded by a bounding box

4.2.2 Distance Computation

Once the lungs have been detected, the next step is to calculate distances of pixels from the detected lung region. The output of this step are *distance images*

computed by applying the distance transform on binary images. These *distance images* are images where the value of each pixel is the distance of that pixel to the nearest pixel belonging to a set of pixels of the object of interest. The distance transform is the operator which works on a binary image to produce the *distance image*. Euclidean distance transform is a transformation using the Euclidean metric [69] and is employed in this study for calculating the pixel distances.

Figures 4.5 shows the formation of the distance images. The first binary image is used to create the distance image which computes the distance of pixels from the detected lung components. The pixels within the lung components are treated as the object pixels and the pixels not belonging to the lung components are treated as the background, thus forming a binary image. The distance transform is applied to the binary image creating a distance image called the ***object*** *distance images*. The second binary image is used to create the distance image which computes the distance of pixels from the bounding box surrounding the detect lungs. All the pixels within the bounding box are treated as object pixels, while pixels outside the bounding box are treated as the background, thus creating a binary image. The distance transform is applied to the resulting binary image creating the ***background*** *distance images*.

4.2.3 Energy Minimization

The energy function to be minimized has been introduced in Chapter 3 is referred to as the *distance-constrained energy* (DCE) and is given as

$$E = \lambda \sum_{p \in \mathbf{P}} R_p + \sum_{\{p,q\} \in \mathbf{N}} B_{p,q} + \sum_{p \in \mathbf{P}} K_p \tag{4.2}$$

The negative log-likelihoods for the regional term in equation (2.4) is calculated from an intensity distribution histogram of the image. This histogram is created using selected pixels called "seeds" marking pixels which belong to the "object"

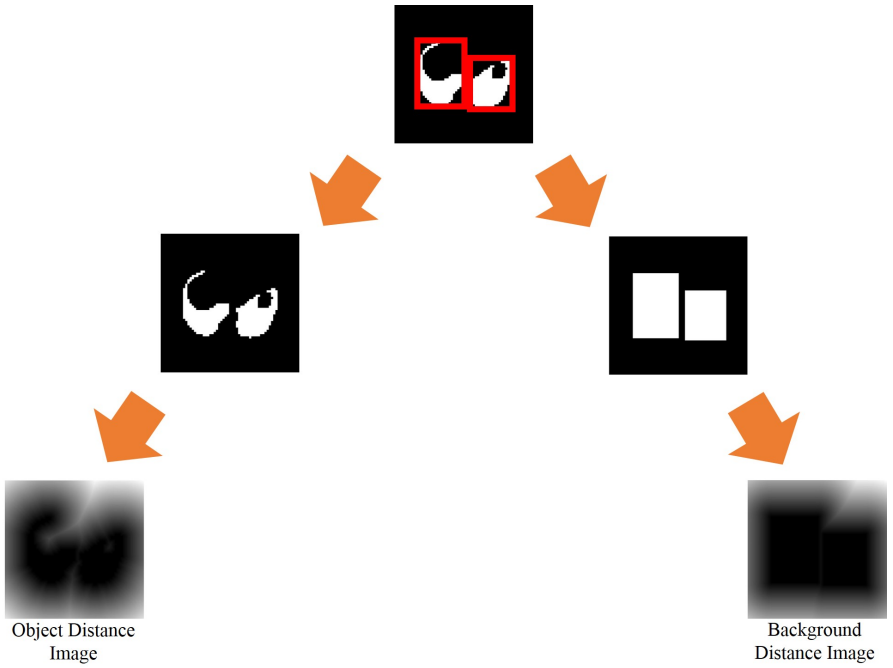

FIGURE 4.5: Formation of the distance images. From the image showing the detected lung component surrounded by a bounding box, two binary images are derived. The distance transform is applied on these binary images to create the object and background distance images

and "background". In [33], the "seeds" are selected interactively by the user. In this work, the seeds are chosen automatically using the knowledge of the absorption rate of x-rays by different parts of the body. The lungs are made of air, and therefore, have low intensity values. The chest structures consisting of bones, fat and soft tissue have intensities ranging from gray to white, and thus, have higher intensity values. Therefore, the seeds selected for the "object" will be the pixels with lowest intensities in the detected lung components, while seeds for the "background" will be the pixels on the border of the bounding box surrounding the detected lung component. To ensure that the pixels selected are representative of the chest structure, this study used three rows of pixels starting from the border of the bounding box and moving outward. This is illustrated in Figure 4.6.

The distance term is estimated from the *distance images* and is calculated using equations (3.2) and (3.3). The boundary term is calculated using equation (2.5).

Figure 4.7(a) shows examples of the result of energy minimization which are binary images showing the pixels labeled as the lungs and pixels not part of the lung

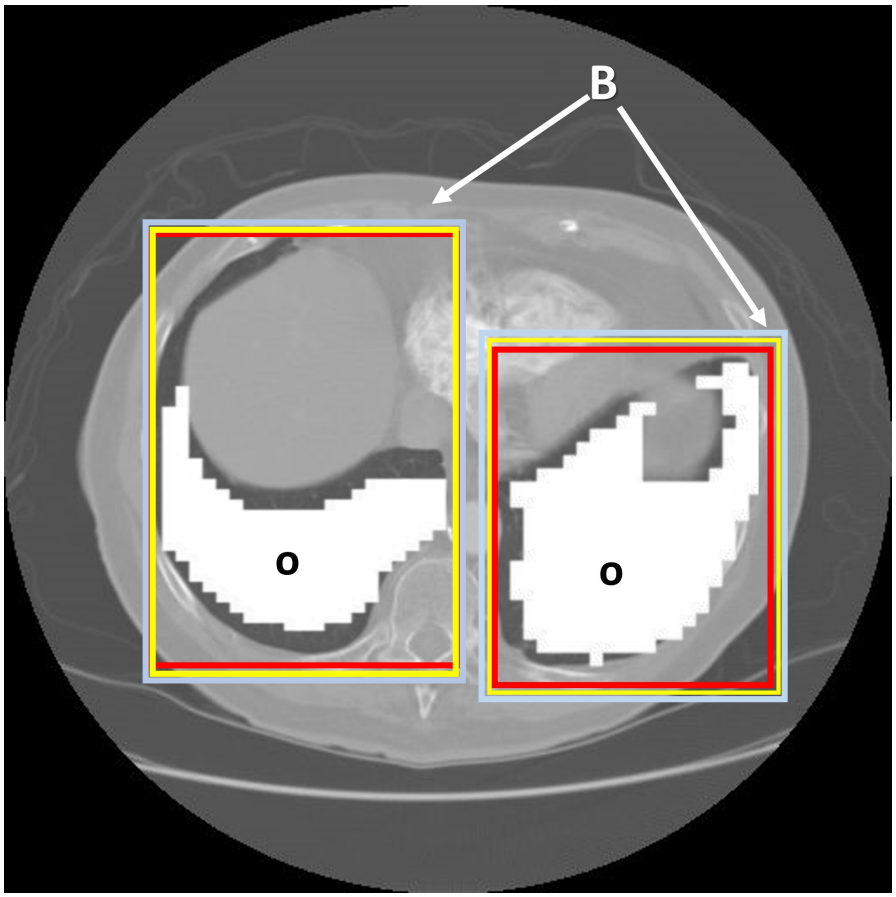

FIGURE 4.6: Seed selection. The object pixels are chosen from the white region marked "O" while the background seeds are chosen from the pixels beneath the three boxes colored red, yellow and blue.

labeled accordingly. The pixels of the lung are labeled with black pixels.

4.2.4 Post Processing

In Figure 4.7(a), the lungs are labeled with black pixels. In the region of black pixels, white specks can be seen. These white specks correspond to high intensity structures within the lungs such as blood vessels and pathology. According to the intensity histogram distribution, the high intensity structures should be assigned different labels from the lungs. However, the goal of segmentation is to extract the lung region in the image, and thus those high intensity structures need to be re-labeled to have the same label as the lung pixels. For this purpose, morphological area opening is employed to correct the mislabeling and targets connected groups

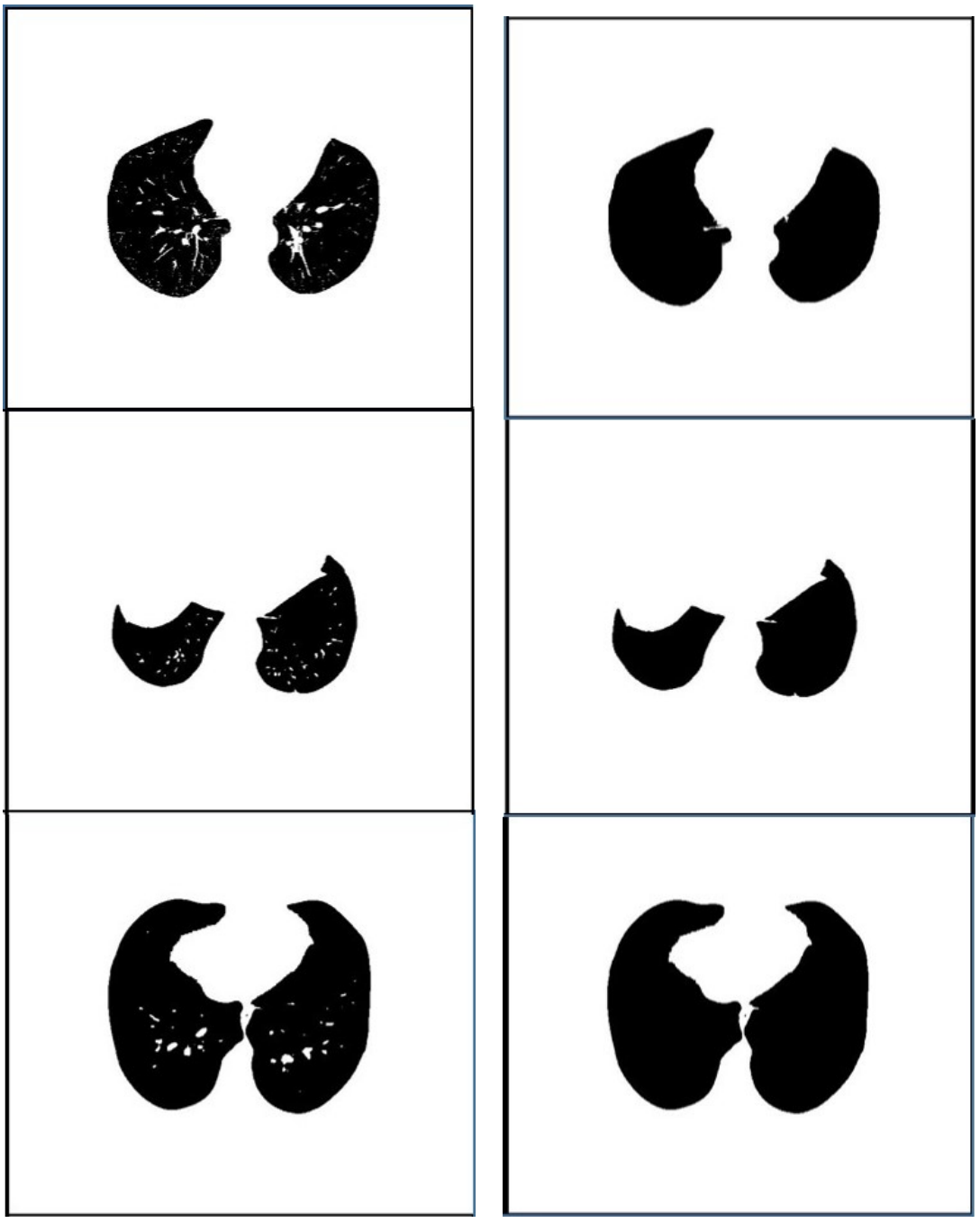

FIGURE 4.7: Examples of the results after energy minimization and after morphological area opening. The black pixels are the labels for the lungs while the white pixels label the background. (a) shows the binary image after energy minimization. (b) shows the mask after morphological area opening

of white pixels smaller than a certain size and eliminates them. Figure 4.7(b) shows the final binary image after morphology.

4.3 Experimental Setup

4.3.1 Performance Metrics

The Dice coefficient, Jaccard similarity and Accuracy are the performance metrics used to evaluate the proposed segmentation method. The Dice coefficient [70] and Jaccard Similarity [71] measure the degree of similarity and overlap between the ground truth (GT) masks and the segmentation results (SR). The performance index ranges from zero to one with an index of zero signifying no overlap between GT and SR while an index of one signifies perfect overlap between them. The Dice coefficient (DC) is given as

$$\mathrm{DC} = 2\frac{|GT \cap SR|}{|GT| + |SR|} \tag{4.3}$$

The Jaccard similarity (JS) is given as

$$\mathrm{JS} = \frac{|GT \cap SR|}{|GT \cup SR|} \tag{4.4}$$

The Dice coefficient and Jaccard Similarity are widely used in evaluating segmentation results and provide a way of comparing the results of this study with other methods in literaure, in addition to evaluating the performance of the proposed method.

The Accuracy is defined in 3.3.2 and calculated using the formula given in equation (3.6).

4.3.2 Experimental Parameters

Each image is split into non-overlapping blocks of size 8×8. Distance thresholds for the distance calculation are as follows: $Th_o = 20$ and $Th_b = 0$. The value of $\lambda = 1$ is used in the DCE. σ in equation (2.5) has been calculated as the variance of the whole image.

4.3.3 Experimental Data

The proposed method is tested on subset of images from each database by comparing ground truth masks with the segmentation results, and calculating the DC, JS and Accuracy for each image. 100 images were selected from LIDC-IDRI, TIME1 and TIME2 databases described in Section 3.3 and used for the experiments. Specifically, 40 images were chosen from LIDC-IDRI and 30 images each were chosen from TIME1 and TIME2 databases. The images in LIDC-IDRI database are arranged in folders according to similar characteristics of the pathology found in each set of image. Therefore, each folder contains a varied mix of images from different patients acquired from CT modality under different conditions. The images in TIME1 and TIME2 contain images from full CT exams of different patients. Each exam is stored in different folders for each patient. In each folder, the images are arranged contiguously from the apex of the lungs to the base. Ground truth masks were created using K-Space segmentation tool set [72] and an atlas showing the anatomy of the chest on a CT image [73].

It was observed that some images from the LIDC-IDRI database posed a challenge to thresholding using the method in [51], and these images were included in the experiments. The images selected from the Lung TIME database are chosen randomly to include the different shapes of the lungs from different locations in the chest region from the axial view, and were selected to investigate the performance of the proposed method on images acquired under different conditions and from CT machines of different manufacturers.

4.4 Experimental Results and Discussion

Table 4.1 shows the performance of the proposed method on images from each of the three databases and the overall performance on all the images used in the experiments and is evaluated using DC, JS and Accuracy. The results presented

in Table 4.1 show that the proposed method has a high performance on the images tested from all the databases. Figure 4.8 shows the performance of the results on some images from the three databases.

TABLE 4.1: Quantitative evaluation using Dice Coefficient (DC), Jaccard Similarity (JS) and Accuracy

Data Set	DC	JS	Accuracy
LIDC	0.9974 ± 0.0011	0.9949 ± 0.0021	0.9953 ± 0.0020
TIME1	0.9970 ± 0.0022	0.9940 ± 0.0043	0.9957 ± 0.0030
TIME2	0.9975 ± 0.0017	0.9949 ± 0.0034	0.9958 ± 0.0025
Mean	0.9973 ± 0.0012	0.9946 ± 0.0024	0.9956 ± 0.0019

Visual results are presented in Figures 4.9, 4.10, and 4.11. Figure 4.9 shows examples of images from the LIDC-IDRI database. Figure 4.10 shows examples of images from TIME1 dataset. Figure 4.11 shows examples of images from TIME2 dataset.

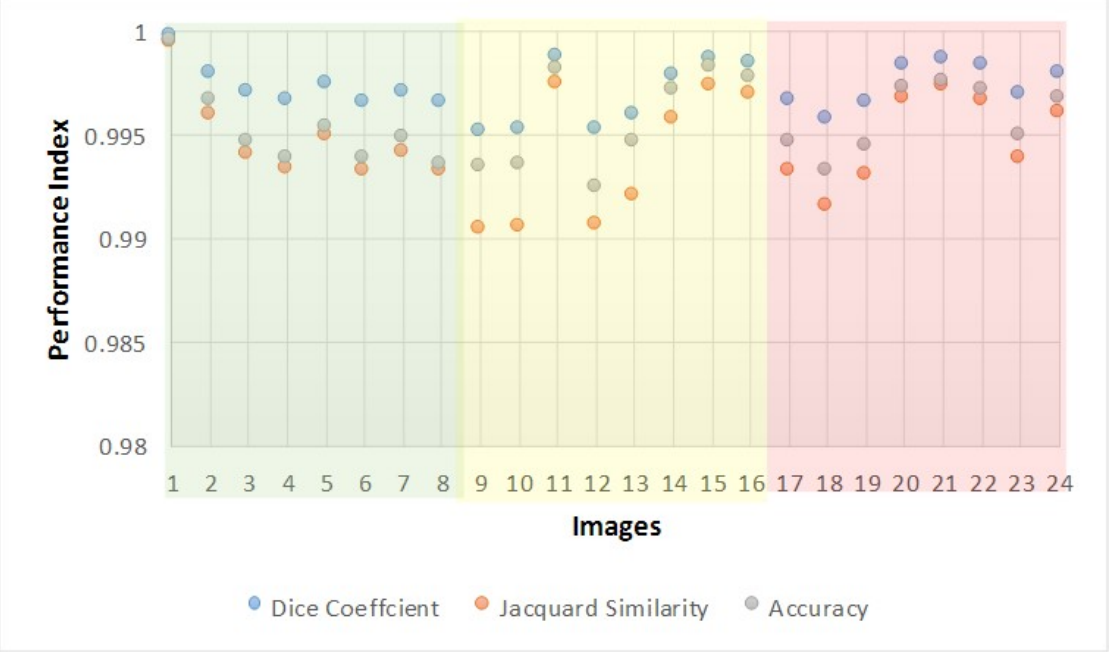

FIGURE 4.8: Performance of the Proposed method evaluated with Dice Coefficient (DC), Jacquard Similarity (JS) and Accuracy on a subset of images from the three databases. Images numbered from 1 to 8 are from LIDC-IDRI database. Images numbered from 9 to 16 are from TIME1 database. Images numbered from 17 to 24 are from TIME2 database

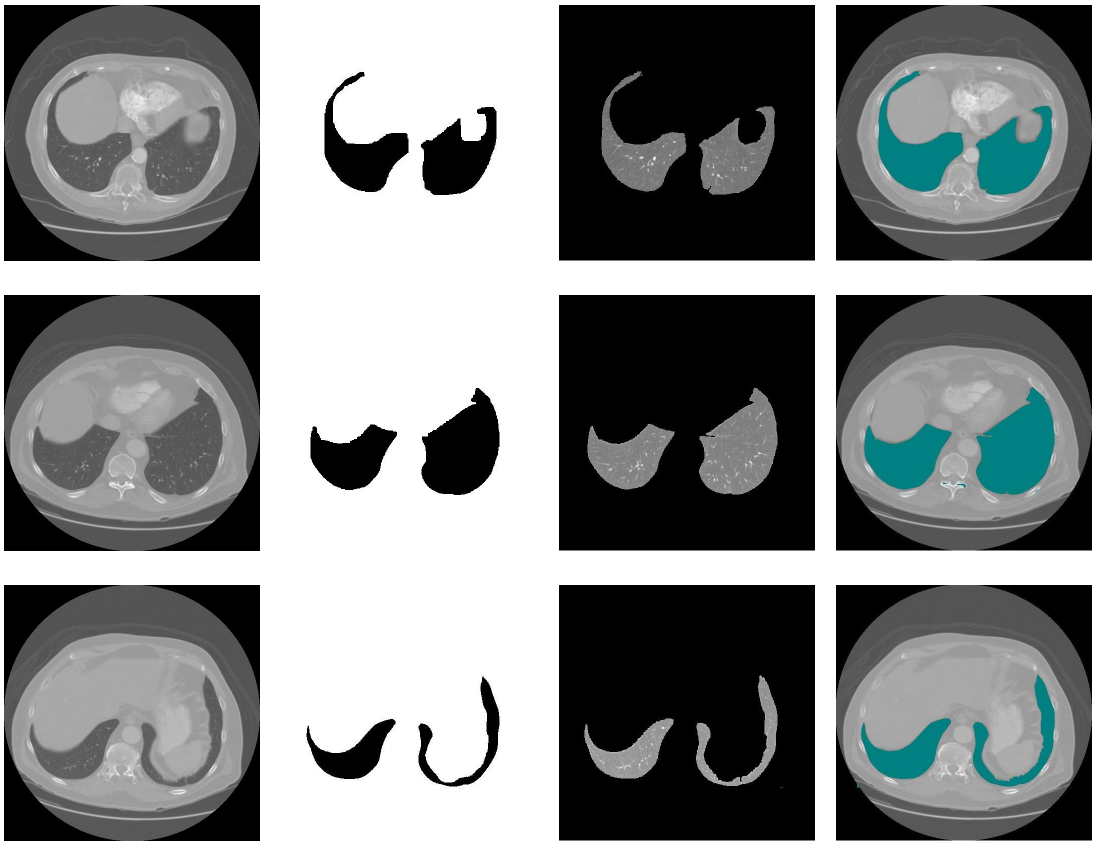

FIGURE 4.9: Examples of segmentation results using the proposed method on images from LIDC-IDRI database. (a) Original Image (b) Ground Truth (c) Segmented Lungs (d) Segmented Lungs overlaid on the Original Image

4.4.1 Comparison with the State-of-the-Art

This section provides an indirect comparison with methods in literature due to the different conditions under which their experiments were carried out. Table 4.2 presents the results of the methods described from literature and compares them with the average results obtained by the proposed segmentation method. The method developed by Massoptier et al. [45] was tested on 168 lung CT slices obtained for clinical purposes and achieved a mean Dice Coefficient index of 97.42% and a distance error of 0.97mm when comparing the segmentation results against manually-delineated images made by an expert. Pu et al. [48] achieved a Jaccard Similarity of $95.1 \pm 2.0\%$ and RMS error of 0.15 ± 0.092 after testing their method on 230 lung CT images from three different sources. The ground truth images were obtained from manual delineations of the images done by a radiologist. Wei

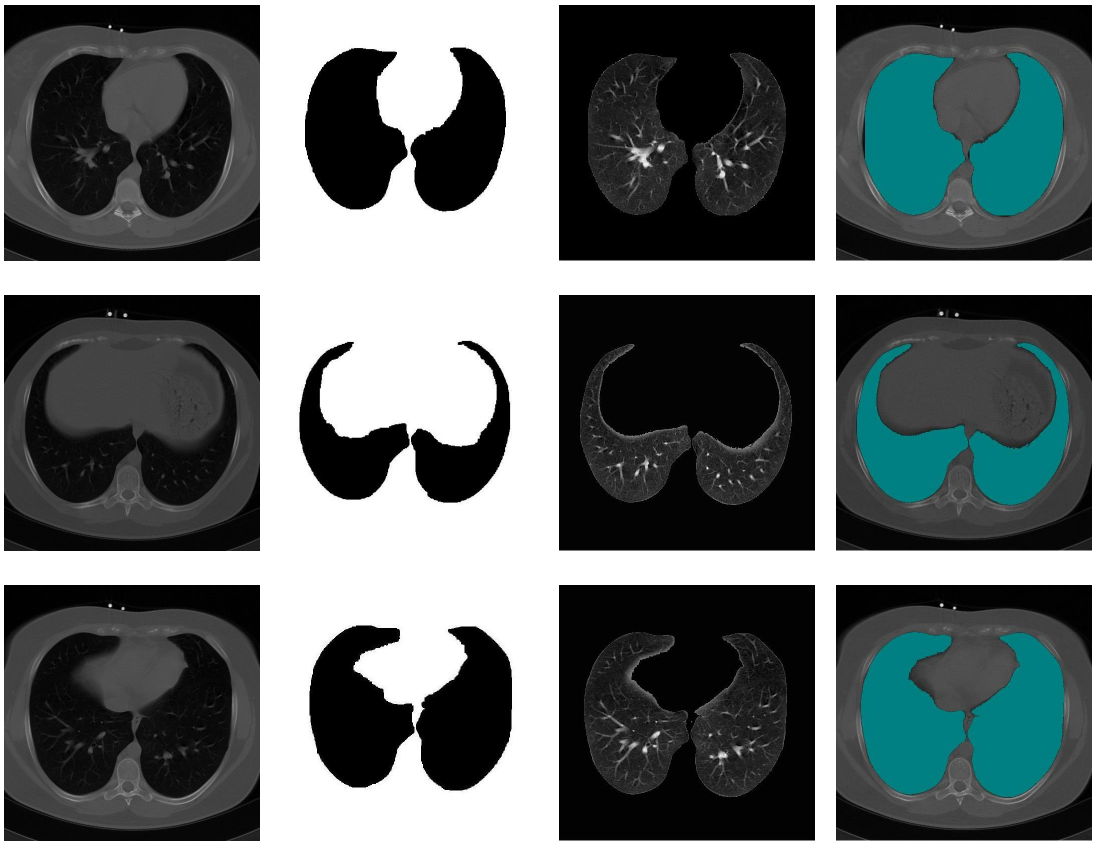

FIGURE 4.10: Examples of segmentation results using the proposed method on images from TIME1 database. (a) Original Image (b) Ground Truth (c) Segmented Lungs (d) Segmented Lungs overlaid on the Original Image

et al. [50] performed the evaluation of their method on two databases. 97 CT images were selected from a Lung Nodule database and 25 scans were selected from a Juxtapleural Nodule Database. They obtained a mean Jaccard Similarity of 95.24% by comparing their segmentation results with gold standards obtained from manually traced contours from three experienced chest radiologists.

TABLE 4.2: Comparison with other methods in the Literature

Method	**JS**	**DC**
Massoptier et al [45]	–	97.42%
Pu et al [48]	$95.1 \pm 2.0\%$	–
Wei et al [50]	95.24%	–
Proposed Method	$\mathbf{99.46 \pm 0.24\%}$	$\mathbf{99.73 \pm 0.12\%}$

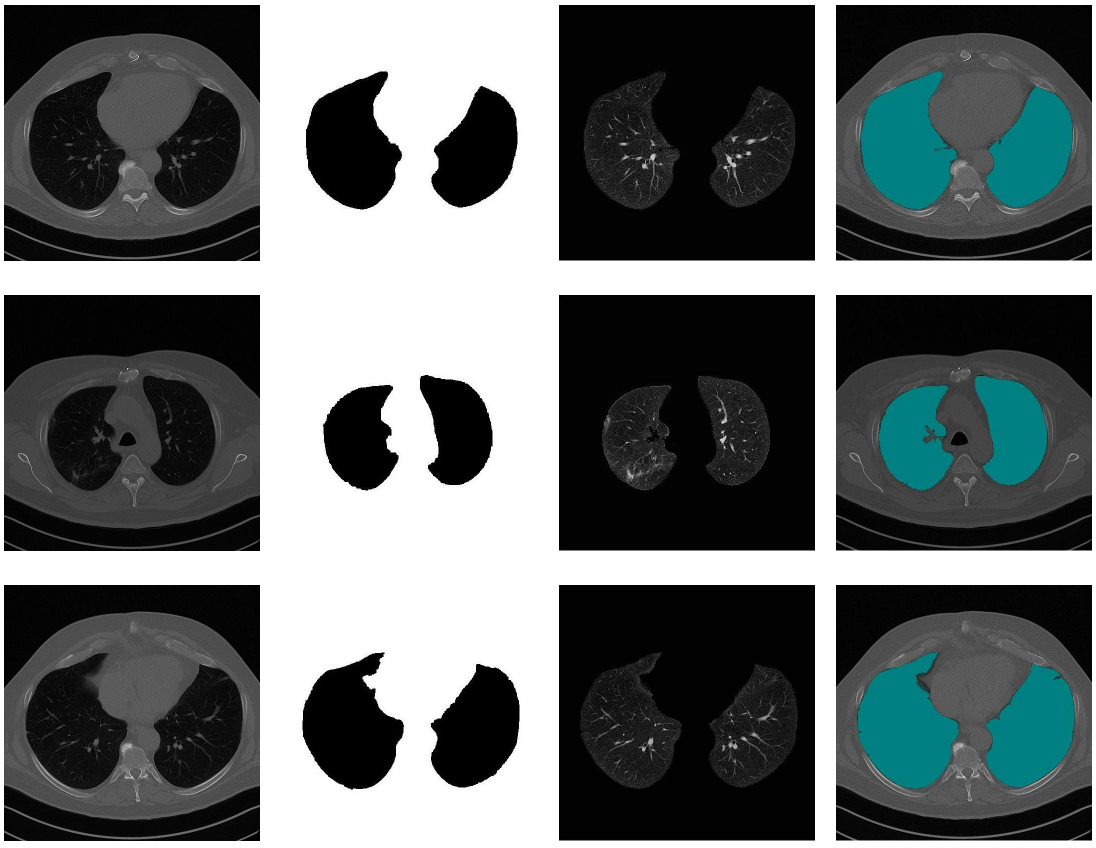

FIGURE 4.11: Examples of segmentation results using the proposed method on images from TIME2 database. (a) Original Image (b) Ground Truth (c) Segmented Lungs (d) Segmented Lungs overlaid on the Original Image

4.4.2 Computation Time

The proposed method was implemented in MATLAB® R2010a using its Image Processing toolbox on a system with Intel Core(TM) i7-4770S @ 3.10Ghz, 8.00GB RAM. The average runtime for an image of size 512×512 is 1.71seconds $\pm$ 0.584. Figure 4.12 shows the average time taken to complete each step. Energy minimization has the highest runtime while morphological area opening has the lowest. The runtime of the detection step has been reduced from about 0.54 seconds to 0.14 seconds by splitting the image into non-overlapping blocks ensuring that FCM algorithm runs on a smaller data size rather than on the original image size. Using FCM on an image of size 512×512 implies that the input data size is $262,144$. However, by splitting the image into non-overlapping blocks of size 8×8, the input data size becomes 4096. Since the distance computation simply

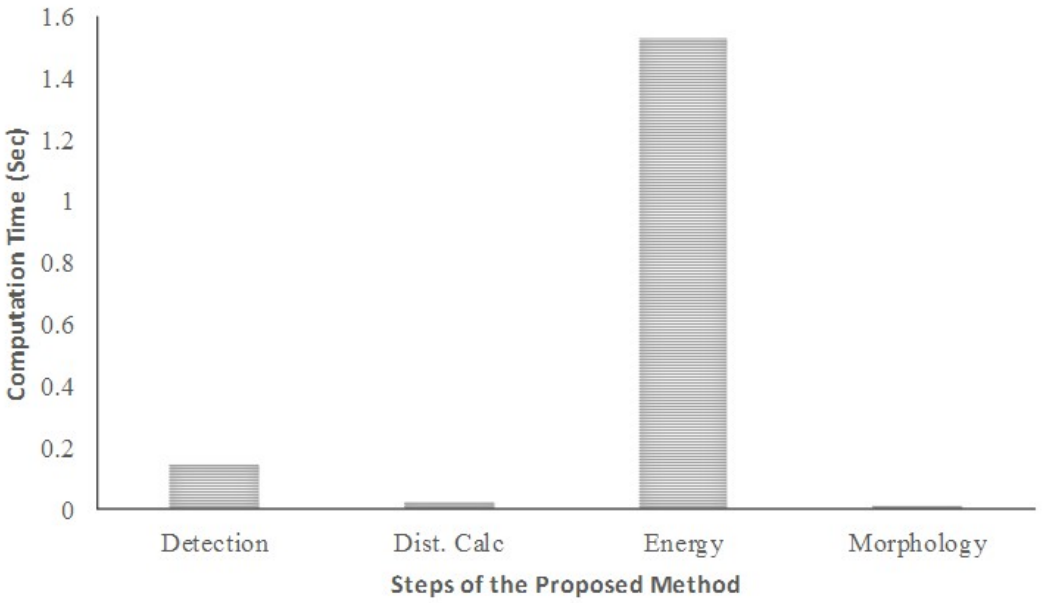

FIGURE 4.12: The average time taken to complete each step of the algorithm

involves applying a distance transform on binary images from the detection step, the runtime is very low.

4.4.3 Effect of block size

The block size affects the accuracy and speed of the region detection step of the proposed method. Figure 4.13 shows an example of the output of clustering as the block size is varied. As the block size increase, it becomes increasing difficult to determine which components belong to the lungs' segment. As can be seen in Figure 4.13(f), thin areas of the lungs get separated at larger block sizes, and gradually disappears. In Figure 4.13(h), the left and the right lung merge together to become a single component. In Figure 4.13(j), the result of the clustering does not yield semantically meaningful partitions. Although progressively increasing the block size increases the difficulty of detecting the lung components from the image, it has advantage of reducing the time taken to complete clustering. This is illustrated in Figure 4.14.

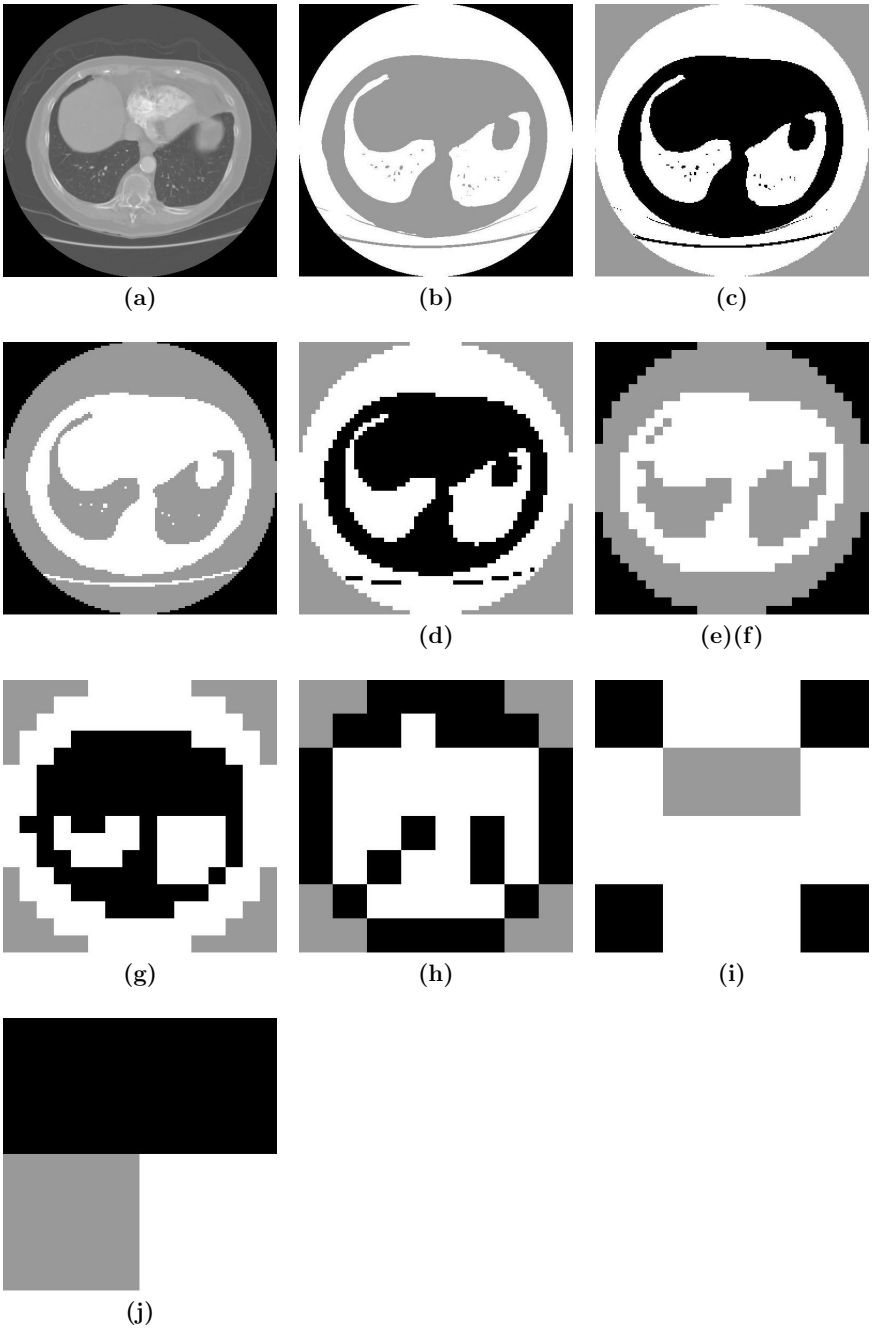

FIGURE 4.13: Example of the output of FCM clustering as the block size is varied in the region detection step (a) Original Image (b) block size = 1×1 (c) block size = 2×2 (d) block size = 4×4 (e) block size = 8×8 (f) block size = 16×16 (g) block size = 32×32 (h) block size = 64×64 (i) block size = 128×128 (j) block size = 256×256

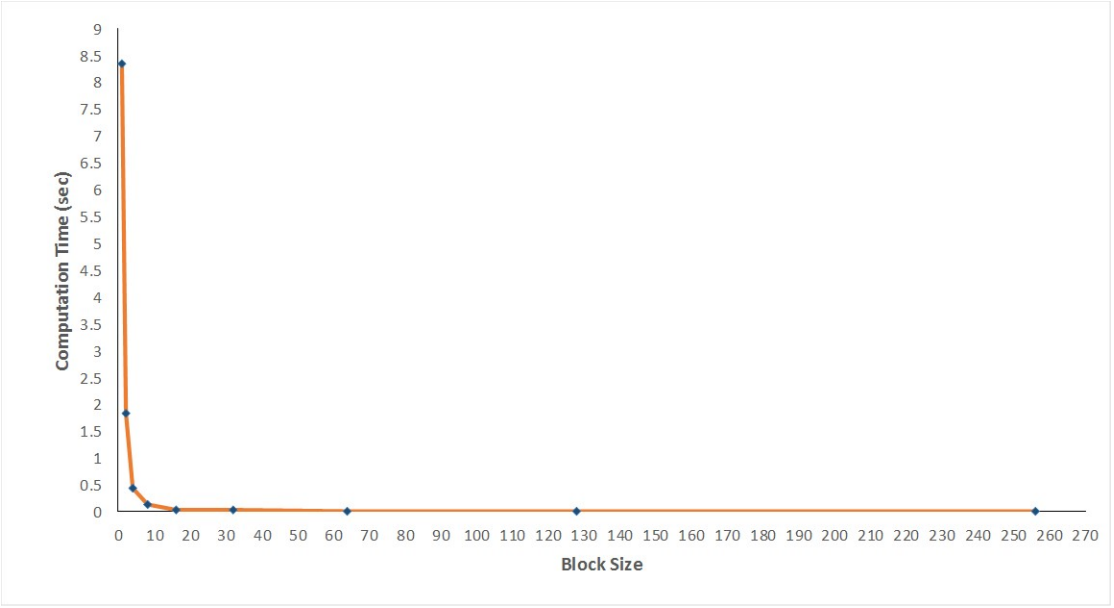

FIGURE 4.14: Graph of FCM clustering computation time against the block size used in splitting the image showing that as the size of the block increases, the computation time decreases.

4.4.4 Images from LIDC-IDRI dataset which pose a challenge to an optimal thresholding method

Figure 4.15 presents the results of images from LIDC-IDRI dataset which did not yield the required result when initially partitioned with the optimal thresholding method in [51]. They were successfully partitioned using the proposed method.

4.4.5 Worst case Examples

There are some cases where the algorithm is unable to isolate the lungs accurately. In some images, the trachea is very close to the lungs causing it to be included in the final results. Another problem is the presence of high intensity structures connected to the boundary of the lungs making it difficult to find the true boundary of the lungs. In other images, the lung boundaries are indistinct and appear blurred, thus making it difficult to find the true lung boundary. Figures 4.16, 4.17 and 4.18 presents some examples of the worst case example. The performance of the proposed method on these images are part of the figures presented in Table 4.1.

4.5 Conclusion

In this chapter, the proposed lung segmentation method has been described. The method includes algorithms for detecting the lung region and calculation of the distance of pixels from the detected region. Subsequent steps of the method include algorithms for the energy formulation incorporating the distance prior, and energy minimization producing the binary labeling of the image. Finally, morphological area opening is used to ensures that all regions within the lungs are included in the final segmentation results. The experimental results have been presented and discussed and show the proposed method gives a high performance and produces highly accurate segmentation of the lungs from a CT image.

The next chapter concludes the dissertation and provides directions for future work.

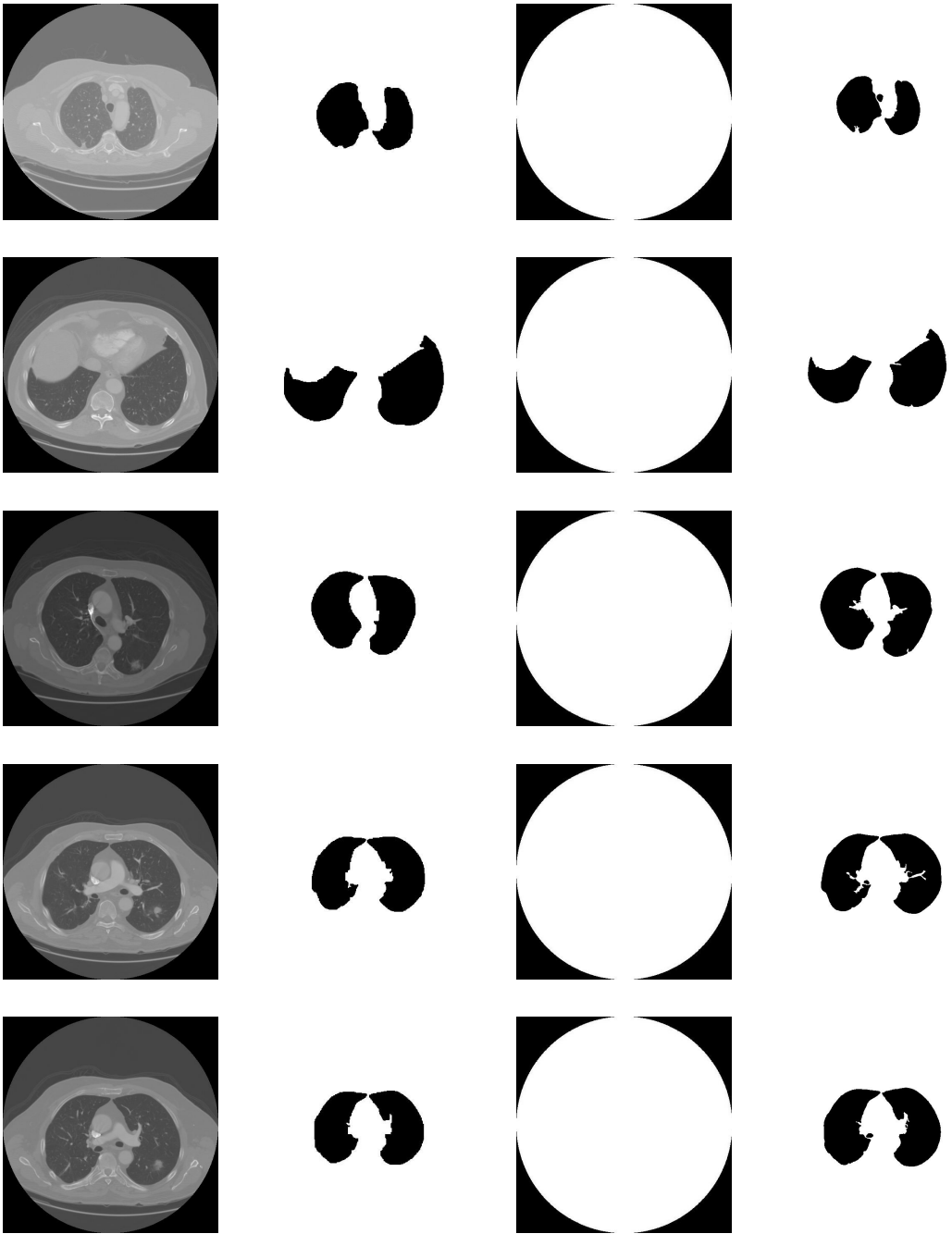

FIGURE 4.15: Segmentation results on images from LIDC-IDRI database which pose a challenge to Otsu thresholding. (a) Original Image (b) Ground Truth (c) Thresholding with Otsu's [51] method (d) Segmented Lungs

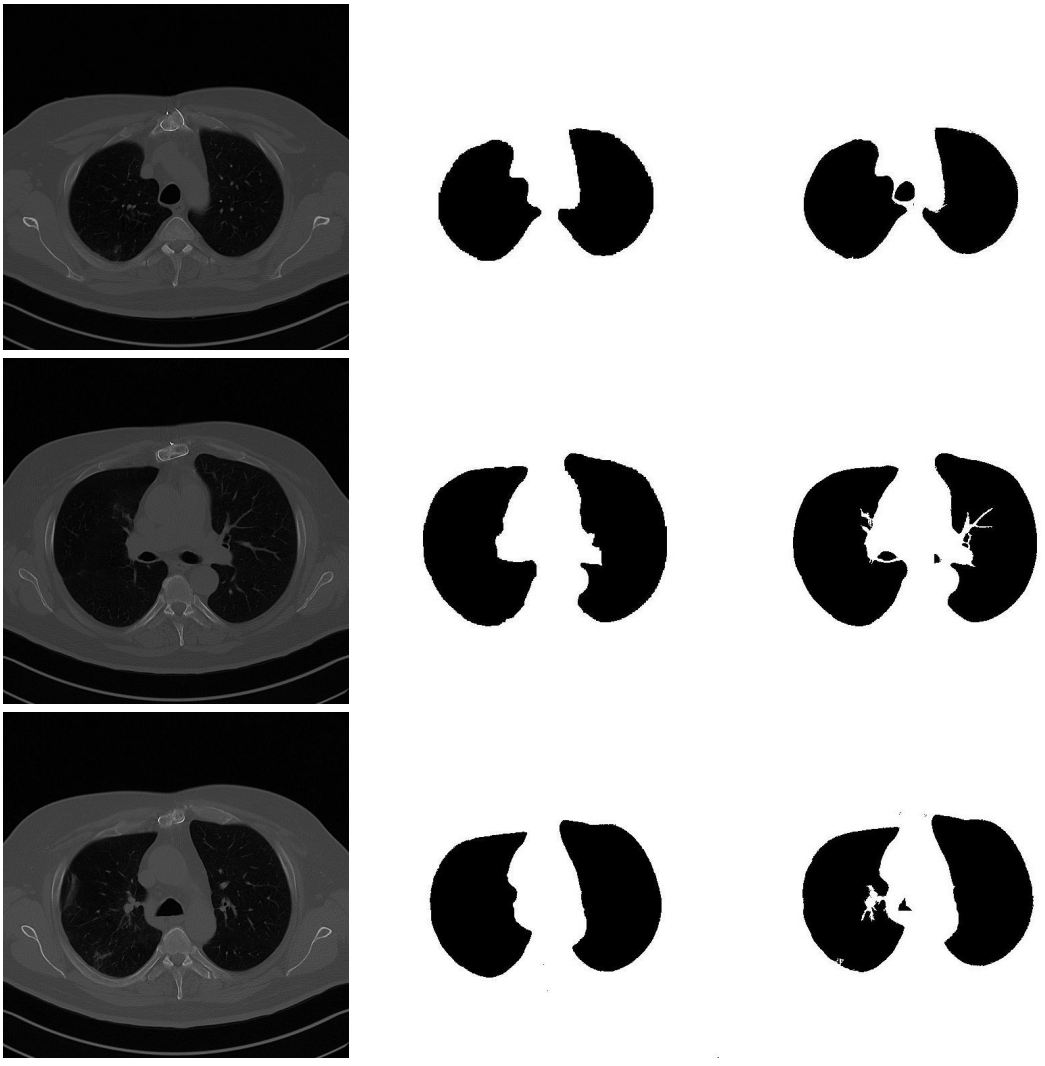

(a) **(b)** **(c)**

FIGURE 4.16: Examples of images showing the failure of the proposed method to exclude the trachea from the segmentation results. (a) Original Image (b) Ground Truth (c) Segmentation Result

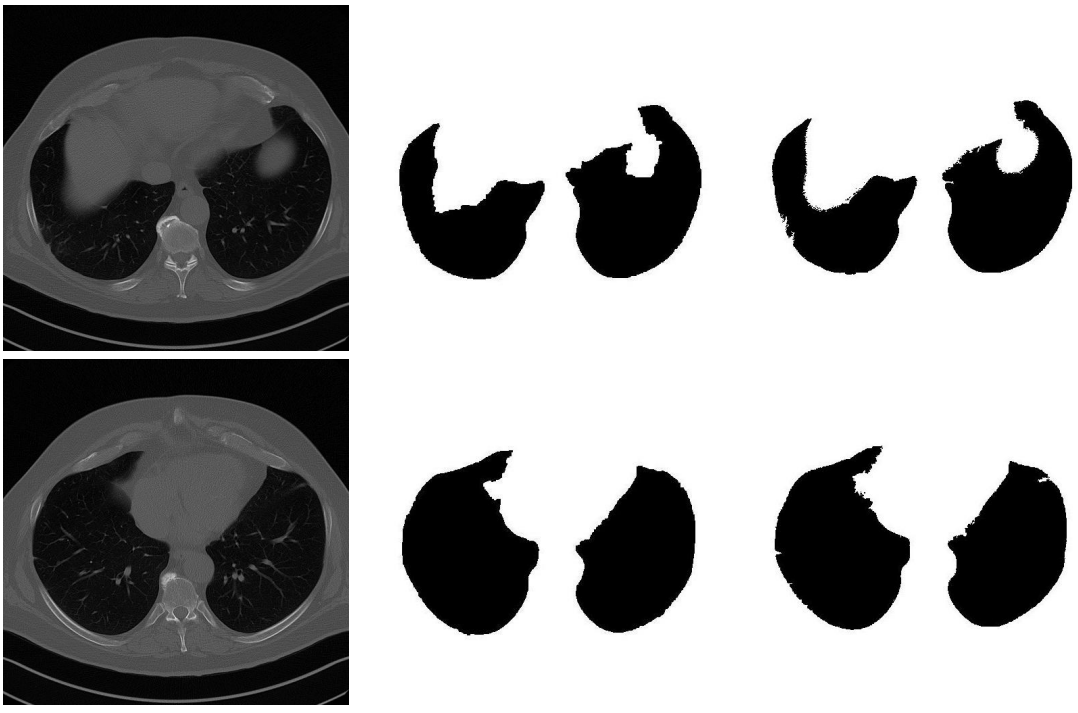

(a) **(b)** **(c)**

FIGURE 4.17: Examples of images showing the failure of the proposed method to accurately segment the boundary of the lungs due to blurred edges of the lungs (a) Original Image (b) Ground Truth (c) Segmentation Result

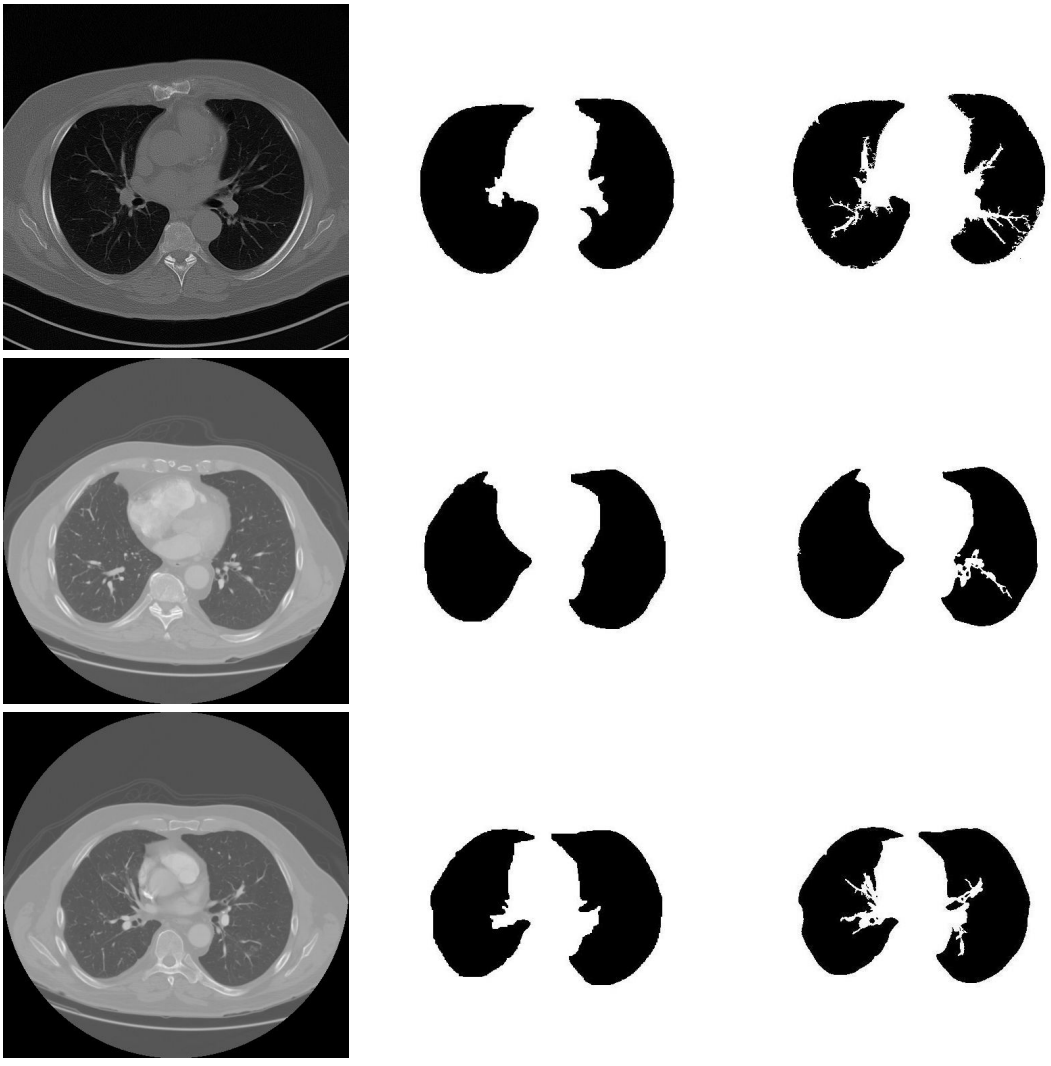

(a) **(b)** **(c)**

FIGURE 4.18: Examples of images where high intensity structures are connected to the lung boundaries. (a) Original Image (b) Ground Truth (c) Segmentation Result

Chapter 5

Conclusion and Future Work

5.1 Conclusion

Segmentation is very important in medical imaging, especially in the area of medical image analysis. Advances in data acquisition technologies have inspired research on ways that Diagnostic Medicine can benefit from the increasing capability of the computers. Early works attempted to make the computer output diagnosis independently, but were met with limited success as it proved difficult to program the complex human thought process into the machine. Recent research has turned towards the use of computers to assist the diagnostic process by acting as a second-opinion while the physician makes the final judgment. The adoption of Computer-aided Detection (CAD) systems has been quite slow due to the high rate of false positive detections which limit the reliability of its output. Therefore, much work still needs to be done to increase the accuracy of the results.

Segmentation is an important step which greatly influences the accuracy of the CAD system. Many studies have been carried out on segmenting the lungs from thoracic CT images. However, many of these methods have only been tested on small image datasets, and thus the performance on a wide range of images acquired from different sources is unknown. In addition, absence of benchmark results

greatly affects the evaluation of these methods which tend to make it subjective to the knowledge of the available expert.

In this dissertation, an automatic segmentation model was proposed using Graph Cut optimization for isolating the lungs' tissues from a CT image, done by incorporating a distance prior as an additional constraint into its energy framework. The distance prior is calculated as the euclidean distance of pixels from the border of the lung region, and thus the first step of the segmentation model involves detecting the lung region. The proposed method does not require the user to select seeds as this is done automatically.

Experiments were carried out to compare between the segmentation results when the Graph Cut energy is used with the distance prior and without the distance prior to determine its suitability as a constraint for restricting the solution space of Graph Cut optimization with the aim of segmenting only the pixels of the lungs. The energy with the distance prior, referred to as the *distance-constrained energy (DCE)*, is then minimized and outputs the binary labeled image with the pixels of the lungs belonging to one class and the rest of the image belonging to another class.

The results obtained from the experiments which compare the segmentation results using the Graph Cut energy with and without the distance prior show that the DCE greatly improves the Specificity and Accuracy of the results while the Sensitivity is largely unchanged. This is because both energy functions were able to accurately identify the pixels of the lungs, which accounts for the Sensitivity index. However, the DCE is also able to isolate the pixels of the lung from pixels with similar intensity to those of the lungs, which accounts for the improvements to Specificity and consequently, the Accuracy indices of the result. These results demonstrate the viability of the distance prior as a constraint enabling the Graph Cut optimization to achieve more accurate lung segmentation results.

The proposed lung segmentation model achieved high performance indices from the experiments carried out using the Dice Coefficient, Jaccard Similarity and

Accuracy performance metrics for evaluation. Specifically, the model achieved a Dice Coefficient of 0.9973 ± 0.0012, a Jaccard Similarity index of 0.9946 ± 0.0024 and an Accuracy of 0.9956 ± 0.0019. The performance of the proposed method is usually affected by the presence of high intensity structures within the lungs attached to the border of the lungs. Compared to the methods in the literature using the same performance metrics, the proposed segmentation model achieved better results.

5.2 Future Work

The proposed model using Graph Cut optimization is able to successfully segment the lungs from CT images. However, its success is dependent on the good choices of parameters in several steps of the method, and therefore, future work will involve finding ways to automatically determine these parameters.

Firstly, the block size used in the image splitting step determines the success of the region detection stage. The smaller the block size, the longer the time to perform clustering and vice versa. Furthermore, the larger the block size, the more difficult it is to detect the lungs from the image. This has been demonstrated in the previous chapter. Therefore, future work will involve finding a suitable algorithm for image splitting or oversegmenting the image. It could also involve finding other algorithms for the image splitting and clustering steps.

Secondly, the clustering method used in this study was FCM. In future studies, the sensitivity of using other clustering methods could be explored. Also, the effect of varying the number of partitions in the image could be examined.

Thirdly, the euclidean distance between pixels was used in defining the distance prior in this study. Future work could include the testing of the sensitivity of the distance prior definitions using other types of distances such as chessboard, city block, or quasi-euclidean.

Fourthly, the energy minimization step has the highest computational cost of all the steps in the proposed method. One reason is that the size of the graph to be constructed affects the speed of the energy minimization. An image of size 512×512 pixels connected with four neighborhood will have about $262,146$ nodes and at least $1,574,916$ vertices. Therefore, future work could involve using efficient methods to reduce the graph size to speed up the computation time and reduce the overhead incurred.

The proposed method was only tested on 100 images from three databases. Future work will involve testing their performance on more images and from other databases.

Bibliography

[1] G. Slabaugh and G. Unal. Graph cuts segmentation using an elliptical shape prior. In *IEEE International Conference on Image Processing, 2005. ICIP 2005.*, volume 2, pages II–1222–5, Sept 2005.

[2] G. Funka-Lea, Y. Boykov, C. Florin, M. P Jolly, R. Moreau-Gobard, R. Ramaraj, and D. Rinck. Automatic heart isolation for CT coronary visualization using Graph-Cuts. In *3rd IEEE International Symposium on Biomedical Imaging: Nano to Macro, 2006.*, ISBI '06, pages 614–617, April 2006.

[3] W. C. RÖNTGEN. On a new kind of rays. *Science*, 3(59):227–231, 1896.

[4] Alexi Assmus. Early History of X Rays. *Beam Line*, 25(2):10–24, 1995.

[5] European Society of Radiology 2009. The future role of radiology in healthcare. *Insights into Imaging*, 1(1):2–11, 2010.

[6] G. N. Hounsfield. Computerized transverse axial scanning (tomography): Part 1. Description of system. *The British Journal of Radiology*, 46(552): 1016–1022, 1973.

[7] O.W. Linton. Medical Applications of X-rays. *Beam Line*, 25(2):25–34, 1995.

[8] I. K. Indrajit and A. Alam. Computer hardware for radiologists: Part I. *Indian Journal of Radiology and Imaging*, 20(3):162–167, 2010.

[9] Peter Mildenberger, Marco Eichelberg, and Eric Martin. Introduction to the DICOM standard. *European Radiology*, 12(4):920–927, 2002.

[10] I. K. Indrajit. Computers in Radiology: Few Recent Advances. *Journal International Medical Sciences Academy*, 26(1):17–20, 2013.

[11] Bradley J. Erickson and Brian Bartholmai. Computer-Aided Detection and Diagnosis at the Start of the Third Millennium. *Journal of Digital Imaging*, 15(2):59–68, 2002.

[12] Phillip H. Meyers, Charles M. Nice, Hal C. Becker, Wilson J. Nettleton, James W. Sweeney, and George R. Meckstroth. Automated Computer Analysis of Radiographic Images. *Radiology*, 83(6):1029–1034, 1964.

[13] R.P. Kruger, James R. Townes, David Lee Hall, Samuel J. Dwyer, and Gwilym S. Lodwick. Automated Radiographic Diagnosis via Feature Extraction and Classification of Cardiac Size and Shape Descriptors. *IEEE Transactions on Biomedical Engineering*, BME-19(3):174–186, May 1972.

[14] Ralph L. Engle Jr. Attempts to Use Computers as Diagnostic Aids in Medical Decision Making: A Thirty-Year Experience. *Perspectives in Biology and Medicine*, 35(2):207–219, 1992.

[15] Kunio Doi. Computer-aided Diagnosis in medical imaging: Historical review, current status and future potential. *Computerized Medical Imaging and Graphics*, 31(4–5):198 – 211, 2007.

[16] Naoki Sakai, Michiaki Mishima, Koichi Nishimura, Harumi Itoh, and Kenshi Kuno. An automated method to assess the distribution of low attenuation areas on chest ct scans in chronic pulmonary emphysema patients. *Chest*, 106 (5):1319–1325, 1994.

[17] Hiroshi Taguchi, Yoshiki Kawata, Noboru Niki, Hitoshi Satoh, Hironobu Ohmatsu, Ryutaro Kakinuma, Kenji Eguchi, Masahiro Kaneko, and Noriyuki Moriyama. Lung cancer detection based on helical CT images using curved-surface morphology analysis. In *Proceedings of SPIE conference on Medical Imaging 1999: Image Processing*, volume 3661 of *Society of Photo-Optical Instrumentation Engineers (SPIE) Conference Series*, pages 1307–1314, 1999.

[18] M.S. Brown, M.F. McNitt-Gray, J.G. Goldin, R.D. Suh, J.W. Sayre, and D.R. Aberle. Patient-specific models for lung nodule detection and surveillance in CT images. *IEEE Transactions on Medical Imaging*, 20(12):1242–1250, Dec 2001.

[19] Dag Wormanns, Martin Fiebich, Mustafa Saidi, Stefan Diederich, and Walter Heindel. Automatic detection of pulmonary nodules at spiral CT: clinical application of a computer-aided diagnosis system. *European Radiology*, 12 (5):1052–1057, 2002.

[20] S.G Armato III and H MacMahon. Automated lung segmentation and computer-aided diagnosis for thoracic CT scans. *International Congress Series*, 1256(1):977 – 982, 2003.

[21] Hidetaka Arimura, Shigehiko Katsuragawa, Kenji Suzuki, Feng Li, Junji Shiraishi, Shusuke Sone, and Kunio Doi. Computerized scheme for automated detection of lung nodules in low-dose computed tomography images for lung cancer screening. *Academic Radiology*, 11(6):617 – 629, 2004.

[22] B. Van Ginneken. Computer-Aided Diagnosis in Thoracic Computed Tomography. *Imaging Decisions MRI*, 12(3):11–22, 2008.

[23] Kenji Suzuki. A review of computer-aided diagnosis in thoracic and colonic imaging. *Quantitative Imaging in Medicine and Surgery*, 2(3), 2012.

[24] Samuel G. Armato, Feng Li, Maryellen L. Giger, Heber MacMahon, Shusuke Sone, and Kunio Doi. Lung Cancer: Performance of Automated Lung Nodule Detection applied to Cancers Missed in a CT Screening Program. *Radiology*, 225(3):685–692, 2002.

[25] Ronald A. Castellino. Computer aided detection (CAD): an overview. *Cancer Imaging*, 5(1):17–19, 2005.

[26] Tomohiro Hirose, Norihisa Nitta, Junji Shiraishi, Yukihiro Nagatani, Masashi Takahashi, and Kiyoshi Murata. Evaluation of Computer-aided Diagnosis (CAD) Software for the Detection of Lung Nodules on Multidetector Row

Computed Tomography (MDCT): JAFROC Study for the Improvement in Radiologists' Diagnostic Accuracy. *Academic Radiology*, 15(12):1505 –1512, 2008.

[27] Marie-Laure Chabi, Isabelle Borget, Rosario Ardiles, Ghassen Aboud, Samia Boussouar, Vanessa Vilar, Clarisse Dromain, and Corinne Balleyguier. Evaluation of the Accuracy of a Computer-aided Diagnosis (CAD) System in Breast Ultrasound according to the Radiologist's Experience. *Academic Radiology*, 19(3):311 – 319, 2012.

[28] Graham Simpson. Thoracic Computed Tomography: Principles and Practice. *Australian Prescriber*, 32(4):105–107, Aug 2009.

[29] The National Lung Screening Trial Research Team. Reduced Lung-Cancer Mortality with Low-Dose Computed Tomographic Screening. *New England Journal of Medicine*, 365(5):395–409, 2011.

[30] Wesley H. Self, D. Mark Courtney, Candace D. McNaughton, Richard G. Wunderink, and Jeffrey A. Kline. High discordance of chest x-ray and computed tomography for detection of pulmonary opacities in ED patients: implications for diagnosing pneumonia. *The American Journal of Emergency Medicine*, 31(2):401 – 405, 2013. ISSN 0735-6757.

[31] Engin Tutkun, Sedat Abusoglu, Hinc Yilmaz, Meside Gunduzoz, Ender Evcik, Türkan Nadir Ozis, Bekir Keskinkilic, and Ali Unlu. Farewell to an old friend: chest X-ray vs high-resolution computed tomography in welders' lung disease. *The Clinical Respiratory Journal*, 8(2), 2014.

[32] D. M. Greig, B. T. Porteous, and A. H. Seheult. Exact maximum a posteriori estimation for binary images. *Journal of the Royal Statistical Society. Series B (Methodological)*, 51(2):pp. 271–279, 1989.

[33] Y.Y. Boykov and M.-P. Jolly. Interactive graph cuts for optimal boundary and region segmentation of objects in N-D images. In *Proceedings of the Eighth IEEE International Conference on Computer Vision, 2001*, volume 1 of *ICCV 2001*, pages 105–112, 2001.

[34] J E Barnes. Characteristics and control of contrast in CT. *RadioGraphics*, 12(4):825–837, 1992.

[35] Julia F. Barrett and Nicholas Keat. Artifacts in CT: Recognition and Avoidance. *RadioGraphics*, 24(6):1679–1691, 2004.

[36] Keita Nakagomi, Akinobu Shimizu, Hidefumi Kobatake, Masahiro Yakami, Koji Fujimoto, and Kaori Togashi. Multi-shape graph cuts with neighbor prior constraints and its application to lung segmentation from a chest CT volume. *Medical Image Analysis*, 17(1):62 – 77, 2013.

[37] Bo Peng, Lei Zhang, and Jian Yang. Iterated graph cuts for image segmentation. In *Proceedings of the 9th Asian Conference on Computer Vision - Volume Part II*, ACCV'09, pages 677–686, Berlin, Heidelberg, 2010. Springer-Verlag.

[38] Human Lung Anatomy. http://pixgood.com/lung-anatomy-bronchioles.html, . Accessed: 2015-01-12.

[39] Shapes and surfaces of the lungs. http://www.getbodysmart.com/ap/respiratorysystem/lungs/shapes_surfaces/tutorial.html, . Accessed: 2015-01-12.

[40] Keith Bridwell. Anatomical Planes of the Body. *SpineUniverse*, 2010.

[41] Thomas. Muttikkal and Chunli. Deng. Azygos Accessory Fissure in Right Upper Lobe Associated with Superior and Inferior Accessory Fissures in Right Lower Lobe. *Journal of Clinical Imaging Science*, 2(1):79, 2012.

[42] Shiying Hu, Eric A. Hoffman, and Joseph M. Reinhardt. Automatic Lung Segmentation for Accurate Quantitation of Volumetric X-Ray CT Images. *IEEE Transactions on Medical Imaging*, 20:490–498, 2001.

[43] Michela Antonelli, Beatrice Lazzerini, and Francesco Marcelloni. Segmentation and reconstruction of the lung volume in CT Images. In *Proceedings of the 2005 ACM Symposium on Applied Computing*, SAC '05, pages 255–259, 2005.

[44] Xiangrong Zhou, Tatsuro Hayashi, Takeshi Hara, Hiroshi Fujita, Ryujiro Yokoyama, Takuji Kiryu, and Hiroaki Hoshi. Automatic segmentation and recognition of anatomical lung structures from high-resolution chest CT images. *Computerized Medical Imaging and Graphics*, 30(5):299 – 313, 2006.

[45] L. Massoptier, A. Misra, and A. Sowmya. Automatic lung segmentation in HRCT images with diffuse parenchymal lung disease using graph-cut. In *24th International Conference on Image and Vision Computing New Zealand, 2009*, pages 266–270, Nov 2009.

[46] Saleem Iqbal and Amir Hanif Dar. Lungs Segmentation by Developing Binary Mask. In *Proceedings of the 7th International Conference on Frontiers of Information Technology*, FIT '09, pages 75:1–75:4, 2009.

[47] M. Arfan Jaffar, Ayyaz Hussain, and AnwarMajid Mirza. Fuzzy entropy based optimization of clusters for the segmentation of lungs in CT scanned images. *Knowledge and Information Systems*, 24(1):91–111, 2010. ISSN 0219-1377.

[48] Jiantao Pu, D. S. Paik, Xin Meng, J. Roos, and G. D. Rubin. Shape Break-and-Repair Strategy and its Application to Automated Medical Image Segmentation. *IEEE Transactions on Visualization and Computer Graphics*, 17(1):115–124, Jan 2011.

[49] N. Mesanovic, M. Grgic, H. Huseinagic, M. Males, E. Skejic, and Smajlovic M. Automatic CT Image Segmentation of the Lungs with Region Growing Algorithm. In *18th International Conference on Systems, Signals and Image Processing - IWSSIP 2011*, pages 395–400, 2011.

[50] Ying Wei, Guo Shen, and Juan-juan Li. A Fully Automatic Method for Lung Parenchyma Segmentation and Repairing. *Journal of Digital Imaging*, 26(3): 483–495, 2013.

[51] Nobuyuki Otsu. A threshold selection method from gray-level histograms. *IEEE Transactions on Systems, Man and Cybernetics*, 9(1):62–66, Jan 1979.

[52] R. Shojaii, J. Alirezaie, and P. Babyn. In *IEEE International Conference on Image Processing, 2005*, ICIP '05.

[53] B. Abdollahi, A. Soliman, A.C. Civelek, X.-F. Li, G. Gimel'farb, and A. El-Baz. A novel Gaussian Scale Space-based joint MGRF framework for precise lung segmentation. In *19th IEEE International Conference on Image Processing, 2012*, ICIP '12, pages 2029–2032, Sept 2012.

[54] Yanhui Guo, Chuan Zhou, Heang-Ping Chan, Aamer Chughtai, Jun Wei, Lubomir M. Hadjiiski, and Ella A. Kazerooni. Automated iterative neutrosophic lung segmentation for image analysis in thoracic computed tomography. *Medical Physics*, 40(8), 2013.

[55] K. Kothavari and S. N. Deepa. Segmentation of Lung on CT images using Robust Active Shape Model (RASM) and Tumour Location using Morphological Processing. *Academic Journal of Cancer Research*, 7(2):73–80, 2014.

[56] Jon Kleinberg and Éva Tardos. Approximation Algorithms for Classification Problems with Pairwise Relationships: Metric Labeling and Markov Random Fields. *Journal of the ACM*, 49(5):616–639, sep 2002.

[57] N. Komodakis and G. Tziritas. Approximate Labeling via Graph Cuts Based on Linear Programming. *IEEE Transactions on Pattern Analysis and Machine Intelligence*, 29(8):1436–1453, Aug 2007.

[58] Martin J. Wainwright and Michael I. Jordan. Graphical models, exponential families, and variational inference. *Foundations and Trends® in Machine Learning*, 1(1–2):1–305, 2008.

[59] Stuart Geman and Donald Geman. Stochastic relaxation, gibbs distributions, and the bayesian restoration of images. *IEEE Transactions on Pattern Analysis and Machine Intelligence*, 6(6):721–741, 1984.

[60] Julian Besag. On the statistical analysis of dirty pictures. *Journal of the Royal Statistical Society Series B*, 48(3):259–302, 1986.

[61] S. Kirkpatrick, C. D. Gelatt, and M. P. Vecchi. Optimization by simulated annealing. *SCIENCE*, 220(4598):671–680, 1983.

[62] L. R. Ford and D. R. Fulkerson. Maximal flow through a network. *Canadian Journal of Mathematics*, 8:399–404, 1956.

[63] Yuri Boykov and Gareth Funka-Lea. Graph Cuts and Efficient N-D Image Segmentation. *International Journal of Computer Vision*, 70(2):109–131, 2006.

[64] M. F. McNitt-Gray, S. G. Armato III, C. R. Meyer, A. P. Reeves, G. McLennan, R. Pais, J. Freymann, M. S. Brown, R. M. Engelmann, P. H. Bland, G. E. Laderach, C. Piker, J. Guo, D. P. Qing, D. F. Yankelevitz, D. R. Aberle, E. J. R. van Beek, H. MacMahon, E. A. Kazerooni, B. Y. Croft, and L. P. Clarke. The Lung Image Database Consortium (LIDC) data collection process for nodule detection and annotation. In *Proceedings of SPIE conference on Medical Imaging 2007: Computer-Aided Diagnosis*, volume 6514 of *Society of Photo-Optical Instrumentation Engineers (SPIE) Conference Series*, pages 65140K–65140K–8, 2007.

[65] M. Dolejsi, J. Kybic, M. Polovincak, and S. Tuma. The Lung TIME: annotated lung nodule dataset and nodule detection framework. In *Proceedings of SPIE conference on Medical Imaging 2009: Computer-Aided Diagnosis*, volume 7260 of *Society of Photo-Optical Instrumentation Engineers (SPIE) Conference Series*, February 2009.

[66] W. Zhu, N. Zeng, and N. Wang. Sensitivity, specificity, accuracy, associated confidence interval and ROC analysis with practical SAS implementations. In *NESUG proceedings: Health care and life sciences*, NESUG 2010, pages 1–9, Nov 2010.

[67] Y. Boykov and V. Kolmogorov. An experimental comparison of min-cut/max-flow algorithms for energy minimization in vision. *IEEE Transactions on Pattern Analysis and Machine Intelligence*, 26(9):1124–1137, Sept 2004.

[68] Oluwakorede Oluyide, Serestina Viriri, and Jules-Raymond Tapamo. A two-Stage Fuzzy c-Means Clustering Algorithm for Lung Segmentation. In *Proceedings of the 2014 PRASA, RobMech and AfIaT International Joint Symposium*, pages 49–52, Nov 2014.

[69] Olivier Cuisenaire and Benoît macq. Fast and exact signed Euclidean distance transformation with linear complexity. In *IEEE International Conference on Acoustics, Speech and Signal Processing*, volume 6 of *ICASSP'99*, pages 3293 – 3296, 1999.

[70] L. R. Dice. Measures of the Amount of Ecologic Association Between Species. *Ecology*, 26(3):297–302, July 1945.

[71] Paul Jaccard. The Distribution of the Flora in the Alpine Zone. *New Phytologist*, 11(2):37–50, February 1912.

[72] Kevin McGuinness and Noel E. O'Connor. The K-Space segmentation tool set. In *3rd International Conference on Semantic and Multimedia Technologies*, volume 3 of *SAMT 2008*, December 2008.

[73] Atlas of CT Anatomy of the Chest.